Preprint typeset using LaTeX style emulateapj v. 11/12/01

FE K EMISSION AND ABSORPTION FEATURES IN THE XMM-EPIC SPECTRUM OF THE SEYFERT GALAXY IC 4329A

A. Markowitz[1,2], J.N. Reeves[1,3], V. Braito[1,3]

[1] X-ray Astrophysics Laboratory, Code 662, NASA/Goddard Space Flight Center, Greenbelt, MD 20771; agm@milkyway.gsfc.nasa.gov; jnr@milkyway.gsfc.nasa.gov
[2] NASA Post-doc Research Associate
[3] Department of Physics and Astronomy, Johns Hopkins University, Baltimore, MD 21218

ABSTRACT

We present a re-analysis of the *XMM-Newton* long-look of the X-ray bright Seyfert galaxy IC 4329a. The Fe K bandpass is dominated by two peaks, consistent with emission from neutral or near-neutral Fe Kα and Kβ. A relativistic diskline model whereby both peaks are the result of one doubly-peaked diskline profile is found to be a poor description of the data. Models using two relativistic disklines are found to describe the emission profile well. A low-inclination, moderately-relativistic dual-diskline model is possible if the contribution from narrow components, due to distant material, is small or absent. A high-inclination, moderately relativistic profile for each peak is possible if there are roughly equal contributions from both the broad and narrow components. Upper limits on Fe XXV and Fe XXVI emission and absorption at the systemic velocity of IC 4329a are obtained. We also present the results of *RXTE* monitoring of this source obtained so far; the combined *XMM-Newton* and *RXTE* data sets allow us to explore the time-resolved spectral behavior of this source on time scales ranging from hours to 2 years. We find no strong evidence for variability of the Fe Kα emission line on any time scale probed, likely due to the minimal level of continuum variability. We detect a narrow absorption line, at a energy of 7.68 keV in the rest frame of the source; its significance has been confirmed using Monte Carlo simulations. This feature is most likely due to absorption from Fe XXVI blueshifted to $\sim$0.1c relative to the systemic velocity, making IC 4329a the lowest-redshift AGN known with a high-velocity, highly-ionized outflow component. As is often the case with similar outflows seen in high-luminosity quasars, the estimated mass outflow rate is larger than the inflow accretion rate, signaling that the outflow represents a substantial portion of the total energy budget of the AGN. The outflow could arise from a radiatively-driven disk wind, or it may be in the form of a discrete, transient blob of ejected material.

Subject headings: galaxies: active — galaxies: Seyfert — galaxies: individual (IC 4329a)

1. INTRODUCTION

The hard X-ray emission of Seyfert 1 AGN is dominated by rapidly-variable emission thought to originate from inverse Comptonization of soft seed photons by a hot corona near the central black hole (e.g., Shapiro, Eardley & Lightman 1976; Sunyaev & Titarchuk 1980; Haardt et al. 1994). Furthermore, the disk, or some other cold, optically thick material, reprocesses the hard X-rays, as evidenced by the so-called 'Compton reflection humps' seen in Seyfert spectra above $\sim$7 keV and peaking near 20–30 keV.

Another signature of reflection is the Fe Kα emission line commonly seen at 6.4 keV; this has proved to be a valuable diagnostic of the accreting material near black holes. A few sources show evidence for a relativistically broadened component that is likely produced in the inner accretion disk, its profile sculpted by gravitational redshifting and relativistic Doppler effects (e.g., Fabian et al. 2002). However, a narrow Fe Kα component is a much more common feature in Seyfert 1s (e.g., O'Brien 2001, Yaqoob et al. 2001). FWHMs of several thousand km s^{-1} are typical (e.g., Yaqoob & Padmanabhan 2004). The narrow component is generally thought to originate in Compton-thick material far from the central black hole, such as the outer accretion disk, the putative molecular torus invoked in standard unification models, or Compton-thick gas commensurate with the Broad-Line Region (BLR).

At the same time, there is strong evidence from X-ray and UV grating observations for the presence of ionized material in the inner regions of a large fraction of AGN (e.g., Blustin et al. 2005). High-resolution spectroscopy shows the gas is usually outflowing from the nucleus; typical velocities are $\sim$ a few hundred km s^{-1}. Absorption due to a broad range of ionic species is commonly seen. For many sources, the relative line strengths argue for several different photoionized absorbing components, as opposed to a single absorber, along the line of sight. In the Fe K bandpass, absorption at 6.7 keV has been seen in NGC 3783 with *XMM-Newton* (Reeves et al. 2004), consistent with absorption by Fe XXV. Additionally, absorption features near $\sim$7–8 keV have been detected in PG and BAL quasars; such features have been attributed to strongly-blueshifted, high-ionization Fe K-shell absorption at near-relativistic ($\sim$0.2c) velocities (Reeves et al. 2003; Pounds et al. 2003a,2003b; Chartas et al. 2002). These features may be signatures of high-velocity accretion disk winds.

IC 4329a is a well-studied, nearby (z = 0.01605) Seyfert 1.2 nucleus embedded in a nearly edge-on host galaxy. It has consistently remained one of the X-ray brightest

Seyfert galaxies for at least a decade. Using simultaneous *ASCA* and *RXTE* data, Done, Madejski & Życki (2001) found the 6.4 keV Fe Kα core to be moderately broadened ($\sim$20,000 km s^{-1} FWHM). The emission was parameterized using a relativistic diskline model, with emission extending inward only to 30–100 gravitational radii R_g. Using a 60 ksec *Chandra*-HETGS observation performed in 2001, McKernan & Yaqoob (2004) detected not only a narrow 6.4 keV core, but also confirmed the presence of emission near 6.9 keV. This double-peaked complex could be fit by several competing models, included dual Gaussians, dual disklines, or a single diskline. Steenbrugge et al. (2005; hereafter S05) observed IC 4329a with *XMM-Newton* for 136 ksec in 2003 (see §2 for details). Their analysis concentrated primarily on the soft X-ray RGS data, which revealed evidence for several absorbing components, including neutral absorption intrinsic to IC 4329a's host galaxy, and a four-component warm absorber spanning a range of ionization states (the log of the ionization parameter ξ ranged from −1.4 to +2.7). Evidence for absorption due to local, z=0 hot gas was also detected. The EPIC-pn data (see below) also detected two emission peaks near 6.4 and 6.9 keV (rest frame), identified as the Fe Kα core and a blend of Fe I Kβ and Fe XXVI emission, respectively. S05 reported that the 6.4 keV line was narrow and did not vary with time, consistent with an origin far from the central black hole.

In this paper, we aim to not only parameterize the Fe K emission due to accreting material in IC 4329a, but also to search for absorption features in the Fe K bandpass that could be indicative of outflowing material. To this end, we have re-analyzed the *XMM-Newton* pn spectrum, concentrating on the Fe K bandpass. We also augment the *XMM-Newton* data with spectra derived from *RXTE* monitoring data to explore time-resolved spectroscopy over a wide range of time scales, search for variability in the Fe K core flux, and parameterize the relation between the core and the flux of the X-ray continuum. The *XMM-Newton* and *RXTE* observations and data reduction are described in §2. Spectral fits to the *RXTE* data are described in §3. Spectral fits to the Fe K bandpass of the *XMM-Newton* EPIC data are described in §4. Time-resolved spectral fitting to the *RXTE* and *XMM-Newton* data are described in §5. The results are discussed in §6, followed by a brief summary in §7.

2. OBSERVATIONS AND DATA REDUCTION

2.1. *XMM-EPIC*

IC 4329a was observed by *XMM-Newton* during revolution 670 on 2003 August 6–7, for a duration of 136 ksec. This paper uses data taken with the European Photon Imaging Camera (EPIC), which consists of one pn CCD back-illuminated array sensitive to 0.15–15 keV photons (Struder et al. 2001), and two MOS CCD front-illuminated arrays sensitive to 0.15–12 keV photons (MOS1 and MOS2, Turner et al. 2001). Data from the pn were taken in Small Window Mode, data from the MOS1 was in PrimePartialW3/large window mode, and data from the MOS2 was in PrimePartialW2/small window mode. The thin filters were used for the pn and MOS2 cameras; the MOS1 used the medium filter. Spectra were extracted using XMM-SAS version 6.50, and using standard extraction procedures. For all three cameras, source data were extracted from a circular region of radius 40″; backgrounds were extracted from circles of identical size, centered $\sim$3′ away from the core. Hot, flickering, or bad pixels were excluded. Data were selected using event patterns 0–4 for the pn. To reduce pile-up, only pattern 0 events were extracted for the MOS cameras. However, we found (e.g., using the SAS task EPAPLOT) that the MOS1 data about 2 keV were severely piled-up; the level of pile-up ranged from $\sim$5–10% at 2–3 keV to $\sim$50% at 10 keV. We do not consider the MOS1 data further in this paper. The MOS2 data above 6 keV suffered from a small level of pile-up, ranging from $\sim$3% at 6 keV to 10% at 10 keV. This reduction yielded 133.3 ksec of pn data, starting at 2003 Aug 06 at 06:57 UTC, and 132.9 ksec of MOS2 data, starting at 2003 Aug 06 at 06:51 UTC. After correcting for deadtime effects, the final exposure times for the pn and MOS2 were 93.2 ksec and 128.8 ksec, respectively. This paper will concentrate primarily on data obtained with the higher signal-to-noise pn, though MOS2 data were also analyzed for consistency. Background-subtracted pn light curves have already been presented in S05. We found a mean 2–10 keV pn count rate of 6.4 c s^{-1}, corresponding to a flux of 8.9×10^{-11} erg cm^{-2} s^{-1}.

Since background flares due to proton flux tend to have hard spectra, the 10–12 keV band of the pn is the band most sensitive to them. The 10–12 keV pn background light curve, plotted in log-space, is shown in Figure 1. To test if these flares had any impact on the pn source spectrum, we filtered out data collected during times when the 10–12 keV background light curve exceeded a count rate of $B + 2\sigma$ (equal to 0.3 c s^{-1}), where B is the mean background rate and σ is the standard deviation of the light curve. This screening yielded a new exposure time of 71.6 ksec. We found that the only major difference was that the screened spectra tended to be fit with a photon index approximately 0.1 steeper than the unscreened spectra, but all other parameters remained virtually unchanged. In particular, the Fe K profile, the focus of this paper, remained unchanged. We therefore concentrated on the unscreened data in all analysis below to increase the signal-to-noise, though we checked the screened data for consistency. However, we note that the brightness of the sources could have an impact on the degree of difference between the screened and unscreened spectra; IC 4329a is an X-ray bright AGN, and for fainter sources, such screening could potentially have a much larger impact than for this dataset. We therefore recommend that the community explore this type of screening as an additional precaution against source contamination from background flares, especially for fainter sources.

2.2. *RXTE observations and data reduction*

IC 4329a has been monitored by *RXTE* once every 4.3 d since 2003 Apr 8 (hereafter referred to as long-term sampling). In this paper, we include data taken up until 2005 Oct 02. Due to sun-angle constraints, no data were taken from 2003 Oct 03 – 2003 Nov 20 or from 2004 Oct 04 – 2004 Nov 21. IC 4329a was subjected to intensive *RXTE* monitoring, once every third orbit (17 ksec) from 2003 Jul 10 to 2003 Aug 13 (hereafter referred to as medium-term sampling; "short-term" sampling refers to the *XMM-Newton*

long-look detailed above). Each *RXTE* visit lasted ∼1 ksec.

2.2.1. *PCA data reduction*

Data were taken using *RXTE*'s proportional counter array (PCA; Swank 1998), which consists of five identical collimated proportional counter units (PCUs). For simplicity, data were collected only from PCU2 (PCU0 suffered a propane layer loss in 2000 May; the other three PCUs tend to suffer from repeated breakdown during on-source time). Count rates quoted in this paper are per 1 PCU. The data were reduced using standard extraction methods and FTOOLS V5.3.1 software. Data were rejected if they were gathered less than 10° from the Earth's limb, if they were obtained within 30 min after the satellite's passage through the South Atlantic Anomaly, if ELECTRON2 > 0.1, or if the satellite's pointing offset was greater than 0.°02.

As the PCA has no simultaneous background monitoring capability, background data were estimated by using PCABACKEST V3.0 to generate model files based on the particle-induced background, SAA activity, and the diffuse X-ray background. The 'L7-240' background models appropriate for faint sources were used. This background subtraction is the dominant source of systematic error in *RXTE* AGN monitoring data (e.g., Edelson & Nandra 1999). Counts were extracted only from the topmost PCU layer to maximize the signal-to-noise ratio. Spectra from individual visits were merged to form a long-term time-averaged spectrum (all data) and a medium-term time-averaged spectrum (intensive monitoring only); total exposures were 278.1 ksec and 100.4 ksec, respectively.

Response matrices were generated using PCARSP V.8.0 over several periods between 2003 and 2005. The PCA response evolves slowly; due to the gradual leak of propane into the xenon layers, the spectral response hardens slowly with time. For example, application of a 2003 matrix to IC 4329a data observed in 2005 (or vice versa) results in a shift in photon index of only ∼0.04. For long-term time-averaged spectral analysis below, a 2004 response matrix was used.

2.2.2. *HEXTE data reduction*

The High-Energy X-Ray Timing Experiment (HEXTE) aboard *RXTE* consists of two independent clusters (A and B), each containing four scintillation counters (see Rothschild et al. 1998) which share a common 1° FWHM field of view. Source and background spectra were extracted from each individual *RXTE* visit using Science Event data and standard extraction procedures. The same good time intervals used for the PCA data (e.g., including Earth elevation and SAA passage screening) were applied to the HEXTE data. To measure real-time background measurements, the two HEXTE clusters each undergo two-sided rocking to offset positions, in this case, to 1.5° off-source, switching every 32 seconds. There is a galaxy cluster (Abell 3571, z = 0.039) located about 2° south of IC 4329a, at R.A. = 13h 47.5m, decl. = –32° 52 m. This source is detected in the *RXTE* all-sky slew survey (XSS; Revnivtsev et al. 2004), which shows the 8–20 keV flux of this source to be about half that of IC 4329a. This suggests that the presence of A3571 could affect HEXTE background determination for any HEXTE cluster which rocks to within roughly 1–2° of the center of A3571 (accounting for the extended size of the galaxy cluster and the ∼1° FWHM collimator response of the HEXTE clusters). However, *BeppoSAX*-PDS observations have shown no detection of A3571 above 15 keV (Nevalainen et al. 2004). The 8–20 keV emission seen by the XSS must therefore be emission only between 8 and $\lesssim$15 keV, and so the presence of A3571 can be safely ignored as far as contaminating the HEXTE background data is concerned. Cluster A data taken between 2004 Dec 13 and 2005 Jan 14 were excluded, as the cluster did not rock on/off source. Detector 2 aboard Cluster B lost spectral capabilities in 1996; these data were excluded from spectral analysis. Cluster A and B data were extracted separately and not combined, as their response matrices differ slightly. Deadtime corrections were applied, and the individual spectra were merged for each cluster to form a long- and medium-term time-average spectrum in the same manner as the PCA data. The net source exposure times for the long-term spectrum were 100.5 ksec (cluster A) and 101.8 ksec (cluster B). Net source exposure times for the medium-term spectrum were 37.0 ksec (A) and 36.5 ksec (B).

3. PCA/HEXTE TIME-AVERAGE SPECTRAL ANALYSIS

We first discuss spectral fits to the long- and medium-term *RXTE* PCA and HEXTE data. The energy resolution of the PCA is low, but we discuss these data first for the purpose of characterizing the broadband hard X-ray continuum and constraining the strength of the Compton reflection component, and applying those constraints to the the high-resolution *XMM-Newton* EPIC data. Additionally, model fits to the long- and medium-term time-averaged spectra were used as templates when analyzing the time-resolved spectra, as described in §5. The medium-term data constitutes a large fraction (36%) of the total long-term data, so the two spectra are not independent.

PCA data below 3.5 keV were discarded in order to disregard PCA calibration uncertainties below this energy and to reduce the effects of the warm absorber (e.g., KS05). For the long-term data, PCA data above 38 keV were excluded as the source counts become dominated by statistical uncertainties at higher energies; in the medium-term data, PCA data above 30 keV were excluded. All PCA data from 24–32 keV were also ignored due to the presence of a feature in the background that is not properly modeled by the current PCA calibration for faint sources (C. Markwardt, priv. comm.).[1] HEXTE data below 25 keV were excluded, as the responses of clusters A and B diverge somewhat for faint sources (N. Shaposhnikov, priv. comm.); there is good agreement above 25 keV. HEXTE data above 100 keV were excluded as the source count rate becomes dominated by statistical uncertainties at higher energies. For the long-term time-average spectrum, HEXTE data above 50 keV were grouped as follows: channels 51–60, channels 61–75, and channels 76 and

[1] As of the time this paper was submitted, the PCA group was preparing to release new background models; testing on IC 4329a showed that the 24–32 keV background features are removed; these data will be included if the new backgrounds are released to the public before the paper is accepted.

above were binned in groups of 2, 3, and 4, respectively. For the medium-term data, data above 39 keV were also binned: channels 39–50 and channels 51 and above were binned in groups of 3 and 8, respectively.

All spectral fitting for both *RXTE* and *XMM-Newton* data was done with XSPEC v.11.3.2l (Arnaud 1996). Errors quoted for spectral fit parameters are 90% confidence. All line energies quoted are for the rest frame unless otherwise indicated. All *RXTE* and *XMM-Newton* spectral fits below included a WABS neutral absorption component. The Galactic column towards IC 4329a is 4.42×10^{20} cm^{-2} (Dickey & Lockman 1990), but previous studies have suggested the presence of additional neutral absorption (e.g., Gondoin et al. 2001). As we did not analyze <2.5 keV *XMM-Newton* pn data or <3.5 keV *RXTE* PCA data, this analysis is relatively insensitive to the precise value of the total (Galactic + intrinsic) neutral column density. We thus left the neutral column density as a free parameter in all fits below.

We first discuss joint fits to the long-term PCA/HEXTE spectra, plotted in Figure 2. In these fits, a constant coefficient was included to account for minor normalization offsets between the PCA and HEXTE. The first model tested, a simple power-law modified by cold absorption (Model 1), yielded large residuals near 6 keV due to the presence of the Fe Kα line; χ^2 was 2129.17/128 degrees of freedom (*dof*). The addition of a Gaussian emission component (Model 2) at 6.38 keV, the Fe Kα line, proved significant at greater than 99.99% confidence in an F-test, since χ^2/dof fell to 586.81/125. However, there still remained broad residuals due to the presence of the Compton reflection component. Model 3 accounted for the presence of this component by using a PEXRAV component to model reflection of an underlying power-law component off optically thick and neutral material (Magdziarz & Zdziarski 1995). The inclination angle i was initially frozen at 30°, and the power-law cutoff energy was kept fixed at 270 keV as per the results of Perola et al. (1999). Elemental abundances were kept fixed at solar. Adding the PEXRAV component proved significant at greater than 99.99% confidence in an F-test, since χ^2/dof fell to 208.14/123. The photon index Γ was $1.894^{+0.013}_{-0.015}$. The reflection fraction R (ratio of the reflection normalization at 1 keV to that of the power law) was 0.51 ±0.04. (With HEXTE data omitted, R from PCA data alone is slightly higher at 0.55±0.07; $\Gamma = 1.908 \pm 0.015$.) For an near face-on inclination ($\cos(i)$ = 0.95), χ^2 increased by 0.1, and R dropped slightly to 0.48±0.04. With the constant coefficient of the PCA fixed at 1.0, the constants for the HEXTE A and B spectra were 0.90 and 0.92, respectively. Table 1 summarizes the model parameters (including line emission parameters) for Model 3. Figure 2 shows the data/model residuals for the three models discussed.

Given the limit of PCA calibration (data/model residuals ~2%[2]) and the high signal-to-noise ratio of this spectrum, systematic errors associated with background modeling and the PCA's spectral response dominated the uncertainties. Finding a statistically-acceptable time-averaged fit (with reduced $\chi^2_\nu \sim 1$) was thus unlikely even if the model was representative of the intrinsic spectrum of the source. Additionally, given the low energy resolution of the PCA (~1 keV at 6 keV), the PCA is largely insensitive to the detailed shape of the Fe Kα line; there were no other obvious residuals seen in the Fe K bandpass. For example, Fe Kβ emission is clearly detected in the EPIC-pn spectrum at 6.90 keV as discussed below, but this is not obvious from the PCA residuals; adding a second Gaussian with rest-frame energy centered at 7.06 keV was only significant at 90% confidence. Additionally, using a diskline model the emission profile (as will be discussed for the EPIC-pn data below) did not provide any improvement in the fit. Model 3 is therefore adopted as a satisfactory fit to the long-term time-averaged PCA/HEXTE spectrum. Since the primary goal of the PCA/HEXTE fitting was to constrain the photon index Γ and the reflection strength R, we will study the more detailed models (adding a second Gaussian to model the Fe Kβ emission; modeling Compton reflection off ionized material; modeling the Fe K emission using relativistic disklines) only using the high resolution EPIC-pn data (§4), checking the PCA spectrum for consistency.

Spectral fitting to the medium-term time average PCA/HEXTE spectrum proceeded in a manner identical to the long-term spectrum, testing the same three models, and with very similar results, although χ^2/dof was lower due to lower signal-to-noise. The results of the Model 3 fit are summarized in Table 1. Compared to the long-term time average spectrum, the medium-term Γ and R are both found to be slightly lower. However, we note the similarity in line emission parameters. Furthermore, the fact that the same type of model is representative of both spectra is consistent with the notion that the general form of the broadband X-ray emission did not change over time.

4. PN FITS

We now focus on spectral fits to the time-average EPIC pn spectrum, shown in Figure 3. The best-fitting model will be used as a template for time-resolved spectroscopic studies in §5. We ignore <2.5 keV data and concentrate only on hard X-ray emission. Additionally, the effective area of the pn drops off rapidly below 2.5 keV. All model fits included absorption by neutral material (WABS model), with the column density left as a free parameter. The unscreened data was used in order to maximize the total good exposure time. §4.1 describes preliminary fits to the data, including attempts to model the Fe K emission using simple Gaussians. §4.2 describes fits using relativistic diskline models. In §4.3, we discuss a narrow absorption feature seen at 7.68 keV, and discuss its detection significance as well as its possible origin. In §4.4, we show that the pn spectrum is consistent with the MOS2 and simultaneous *RXTE* spectra.

4.1. *Fe Kα and Kβ emission: preliminary fits*

Model 1, consisting of a simple power law, yielded a statistically unacceptable fit with large data/model residuals which clearly indicated the presence of an emission line near 6.4 keV (the Fe Kα core) and a rise in the continuum above 7 keV (Compton reflection hump). Data/model residuals for the best-fit model are shown in Figure 3. For Model 2, a narrow Gaussian was added to model the Fe Kα line; the best-fitting energy is 6.40±0.01 keV, and the core

[2] See http://lheawww.gsfc.nasa.gov/users/keith/rossi2000/energy_response.ps

width σ_1 is 112+19$_{-15}$ eV. However, there were still significant data/model residuals near 7 keV suggesting additional line emission, and residuals in the continuum above 7 keV which suggested that the Compton reflection hump is detected independently of the Fe Kα core. For Model 3, a PEXRAV component was added, with R fixed at 0.51, the value from the long-term *RXTE* PCA/HEXTE fits above. The high-energy cutoff was fixed at 270 keV (e.g., Perola et al. 1999); solar metal abundances and an inclination of 30° were assumed. The best-fitting model had χ^2/dof = 1865.73/1893, but data/model residuals, shown in Figure 4, indicated strong, narrow excess emission near 7.0 keV as well as a deficit near 7.7 keV which suggested an absorption feature of some kind. The best-fit spectral parameters for Models 1–3 are listed in Table 2. As an independent confirmation of the edge at 7.1 keV, we fitted the pn data with an edge instead of a PEXRAV component. We found an edge energy of 7.16±0.07 and an optical depth of 0.05±0.01, similar to the results found by Gondoin et al. (2001).

We hypothesized that the emission near 7.0 keV (the "blue peak"; "red peak" refers to the 6.4 keV line) could be due to Fe Kβ, H-like Fe K, or a blend of both. Accordingly, Model 4 featured the inclusion of a second Gaussian component near 7.0 keV. The best fit had a blue peak with energy centroid at $6.93^{+0.09}_{-0.10}$ keV and a width σ_2 of 121^{+95}_{-59} eV. The energy centroid of the Kα Gaussian did not change, though the Kα width σ_1 decreased slightly to 91± 13 eV. The best-fit χ^2/dof was 1844.88/1890. Using an F-test to assess the significance of adding this component yielded a null hypothesis probability of 9.36×10^{-5}. Data/model residuals are plotted in Figure 4; the best-fit spectral parameters are listed in Table 2.

In this model, the red peak centroid energy, 6.39±0.01 keV, is consistent with Kα emission from neutral (or at best mildly-ionized) Fe. The core width σ_1, 91±13 eV, corresponds to a FWHM width of 210 ± 30 eV, or a FWHM velocity of 9700 ± 1400 km s^{-1}. This value is consistent with that derived using *Chandra-HETGS*, 15100^{+12400}_{-10000} km s^{-1} (Yaqoob & Padmanahban 2004). We note that the 6.4 keV line is resolved at the pn resolution of ~140 eV: fixing σ_1 at 1 eV caused large data/model residuals to appear between 6.0–6.6 keV while χ^2 increased by 91. Similarly, the blue peak is also resolved by the pn. Fixing σ_2 to 1 eV caused χ^2/dof to increase to 1851.40/1891, significant at 99.0% confidence in an F-test.

Given the energy resolution of the pn, it was not obvious from these parameters whether the emission line is due to neutral (or only mildly-ionized) Fe Kβ at 7.056 keV, Fe XXVI at 6.966 keV, or a blend of both. For example, fixing σ_2 to be equal to σ_1, as would be expected if the 7.0 keV emission is due entirely to Fe Kβ, resulted in very little change in χ^2 (–0.86), and virtually no change in any other model parameter; i.e., it was not significant to thaw σ_2. To test if the blue peak was consistent with being due solely to neutral Fe Kβ emission, we adjusted Model 4 as follows: we fixed the blue peak's centroid energy at 7.06 keV and fixed the ratio of the Kβ/Kα fluxes at 17/150. The width σ_2 was kept tied to that of the Fe Kα core, σ_1. The best fit model (Model 5) showed virtually no change in the 6.4 keV core or continuum model parameters compared to Model 4 (see Table 2). However, the fit was slightly worse: χ^2/dof was 1852.78/1893, and, as shown in Figure 4, small data/model residuals appeared near 6.8 keV, signifying excess unmodeled emission on the red side of the blue peak.

As shown in Figure 4, the data/model residuals for Models 4 and 5 suggested unmodeled emission on the red side of the Kα line 6.1 keV, prompting us to test for the presence of a Compton-scattering shoulder. Such a feature might be expected at 6.24 keV due to Fe Kα photons Compton-scattering on electrons in the medium in which the line is formed. The ratio of the shoulder and core intensities indicates scattering in, and an origin for the Fe Kα line in, Compton-thick or Compton-thin material (ratio above or below ~0.1–0.2, respectively; see Matt 2002 for further details). Building on Model 4, the better-fitting of the double-Gaussian models, we added a third Gaussian emission component with centroid energy fixed at 6.24 keV and a core width tied to that for the 6.4 keV core (Model 6A). The best-fit model had a χ^2/dof of 1839.03/1889, and an equivalent width EW of 11±8 eV. An F-test showed it was significant at 98.6% to add this component, however, the change in χ^2 compared to Model 4 was only 5.85. Thawing the centroid energy (Model 6B) resulted in a modest improvement in the fit; χ^2/dof dropped to 1833.68/1888 as the centroid energy moved to now $6.13^{+0.07}_{-0.25}$ keV. Best-fit spectral parameters for Model 6A and 6B are listed in Table 3. According to an F-test, it was significant at 98.1% confidence to thaw the centroid energy. Considering the pn energy resolution, this feature does not seem entirely consistent with emission from a Compton shoulder.

4.2. *Fe Kα and Kβ emission: diskline fits*

We now discuss whether relativistic diskline models (Laor 1991) can describe the Fe K profile of IC 4329a. Done et al. (2000) noted from the *ASCA* observation that IC 4329a does seem to have a slightly broadened red wing, though not as broad as that of the "archetypal" broad line source, MCG–6-30-15 (Tanaka et al. 1995); see Figure 2 of Done et al. (2000). Their best-fitting models for the broad emission suggested that there was not significant line emission at radii smaller than ~30–100 R_g ($R_g = GM_{BH}/c^2$). However, compared to the *ASCA* data, the pn spectrum reveals additional emission and absorption features in the Fe K band, prompting us to probe if diskline models can successfully account for all of the emission/absorption features in the Fe K bandpass.

As seen by McKernan & Yaqoob (2004), the approximate heights above the power-law continuum of the red and blue peaks in the 60 ksec HEG spectrum were approximately equal, with the blue peak possibly slightly higher. This prompted McKernan & Yaqoob (2004) to test whether the two peaks could be horns from the same diskline model. Their best-fit model was one with an inclination angle of $24^{+9\circ}_{-1}$, rest-frame line energy of $6.74^{+0.22}_{-0.13}$ keV, a flat radial emissivity profile ($\beta < 0.7$, where the radial emissivity per unit area is quantified as a power law, $r^{-\beta}$), and emission between ~6 and 70 R_g. However, the current EPIC-pn spectrum clearly shows that the EW and height above the power-law continuum of the red peak are much greater than those of the blue peak. A relativistic diskline model with near face-on inclination, e.g., $\lesssim$10°, can typically produce only one peak, and thus one

diskline cannot account for both peaks simultaneously. A diskline model with intermediate or high inclination angles is required to produce two peaks; usually the blue horn is much larger than the red horn unless the disk is truncated at ~tens of R_g and/or the radial emissivity profile is relatively flat. We attempted to fit such a model to the Fe K profile in the pn data. Model 7 consisted of a power-law, a PEXRAV component, and a LAOR diskline component. We tested inclination angles of 30°, 50°, and 70°. The outer radius R_{out} was kept fixed at 400 R_g. The inner radius R_{in} was kept free, but in all fits, R_{in} went to very large values, usually 250–350 R_g, with very poor constraints. Several values of the emissivity index β were tested (1, 2, 3, 5, 7), but all fits yielded poor or no constraints on β. In all cases, there were large systematic data/model residuals across the Fe K bandpass, as shown in Figure 4 (see also Table 4). The values of χ^2 for best-fit models were typically 1920–2140 for 1893 *dof*, significantly worse fits than e.g., the double-Gaussian model. We conclude that a single-diskline model is an inaccurate description of the data.

The unmodeled excess emission near 6.1 keV and 6.8 keV in the double-Gaussian model (Model 5) potentially signified that the Kα and Kβ emission components could each be independently modeled better using a redward asymmetric, moderately relativistic diskline profile instead of a symmetric Gaussian profile. McKernan & Yaqoob (2004) tested dual-diskline models for the HEG spectrum; the best-fit model was one with a nearly face-on inclination $i < 6°$, a moderately steep emissivity index $\beta = 2.4\pm0.2$, and emission spanning the radii between 6 R_g (fixed) to 600 R_g. S05's best fit double-diskline model was found to be consistent with this; β was < 1.4, an inclination angle <17°, a profile that is very similar to the double-Gaussian model. We also fit a double-diskline model to the data, with i, β, R_{in}, and R_{out} for the red and blue disklines set equal to each other, and the normalization of the blue diskline equal to 17/150 that of the red diskline. R_{out} was kept fixed at $400R_g$; it was not significant to thaw this parameter. Our best fit model (Model 8, see Table 5) agrees generally well with that of S05; we found $i = 1^{+11}_{-1}°$, $\beta = 2.1\pm0.3$, and $R_{in} = 13^{+13}_{-11.5}$ R_g. The energy of the red peak was $6.44^{+0.02}_{-0.01}$ keV, more consistent with Kα emission from mildly ionized Fe than from neutral Fe. The blue peak energy was 6.98±0.09 keV, consistent with Kβ emission from neutral or mildly-ionized Fe. The equivalent width $EW_{K\alpha}$ of the Fe Kα line in this model is 86^{+17}_{-8} eV. The values of $EW_{K\alpha}$ and Compton reflection strength R were consistent with the prediction of George & Fabian (1991) that, for reflection off neutral material, the reflection strength R will be equal to $EW_{K\alpha}$ / 150 eV.

As shown in Figure 4, the dual-diskline model accounts well for all of the excess emission-like residuals near 6.0 and 6.8 keV, but it does not account for the 7.7 keV absorption-like residuals, which still persist. The value of χ^2/dof for this model was 1835.02/1890, i.e., the value of reduced χ^2 is slightly lower than that for the Compton shoulder model, 6B. The fact that the 6.1 and 6.8 keV residuals are now well modeled suggests that this model is a better description of the data compared to the double Gaussian models. To quantify this statement, we replaced only the red peak Gaussian in Model 5 with a LAOR component and refitted. χ^2/dof fell to 1843.92/1890, significant at 97.2% confidence in an F-test compared to Model 5. Replacing only the blue peak Gaussian with a LAOR component and refitting yielded χ^2/dof=1846.48/1889, significant at only 83.1% confidence in an F-test compared to Model 5. Additionally, the fact that Model 8 takes care of the ~6.0 keV residuals suggests it is a better fit than models with a Compton shoulder. In fact, adding a Gaussian in emission at 6.24 keV to Model 8, we found only an upper limit of 6 eV to Compton shoulder emission, e.g., we conclude that do not detect the Compton shoulder with high significance.

A LAOR profile assumes a maximally-rotating Kerr black hole. Substituting the LAOR model components with DISKLINE model components and assuming a non-rotating Schwarzschild black hole (Fabian et al. 1989), into the model yields a very similar fit to Model 8 (χ^2/dof = 1839.36/1890); one would not expect significant differences in the line profile unless there was significant emission originating from within a few R_g of the black hole. Almost all DISKLINE best-fit parameters were virtually identical to the LAOR parameters, though the inclination was slightly higher ($i = 14^{+6}_{-4}°$). For the remainder of this paper, "diskline" will denote the LAOR model only.

Another possible diskline model is one wherein the Doppler horns are very close together and unresolved by the pn. A flat emissivity profile and an inclination angle of ~20–30° can yield such a profile for certain ranges of β and R_{in}. Additionally, the blue horn in this profile is slightly higher than the red horn; the fact that the best-fitting rest-frame energy for the Fe Kα diskline in Model 8 was 6.44±0.01 suggests that this model is worth exploring. Inclination angles much higher than ~30° yield line profiles with Doppler peaks that could be resolved by the pn. We tried applying such a model to the data, fixing the inclination angle to values in the range 20–30 °. However, these models could not account for the peak of the emission and the broad red wing simultaneously. Values of χ^2/dof generally stayed about 1900/1891, and we conclude that this model does not describe the emission profile as well as Model 8 above.

Finally, we explored the possibility that there could be additional contributions to the emission profile from narrow Fe Kα and Kβ lines, as would be expected if there is non-negligible Fe K emission originating in material far from the black hole. We added two narrow Gaussians to Model 8 at the rest-frame energies for Fe Kα and Kβ, with the Kβ normalization set to 17/150 times that of the Kα line. We first considered the possibility that each broad component is described by a low-inclination diskline component, similar to that used in Model 8. We kept the widths of both peaks fixed at 50 eV. The best-fit model (referred to as Model 9A hereafter) is one with diskline parameters nearly identical to those in Model 8, with the Kα and Kβ lines contributing only a small amount, and formally consistent with upper limits only in EW. The best-fit parameters are listed in Table 6. Compared to Model 8, χ^2 decreases by only 1.2 for one additional *dof*. Data/model residuals look identical to those in Model 8 and are not plotted. The maximum allowable EW for the narrow Kα line, without significantly changing any of the diskline parameters, is 27 eV; for this case, the EW of the broad Kα line is 54 eV. We conclude that if the

two broad components are described by low-inclination, moderately-relativistic disklines, then the bulk or entirety of the emission must be from the broad component, but a contribution from two narrow components cannot be ruled out.

We next considered the possibility that for each peak, a high-inclination broad line component is present and responsible primarily for the red-wing emission, with a narrow component accounting for the bulk of the peak emission very close to 6.40 or 7.06 keV. We kept the rest-frame energies of the Fe β broad and narrow components fixed at 7.06 keV. Parameters for the best-fit model (henceforth referred to as Model 9B) are listed in Table 6. The best-fitting χ was nearly identical to that for Model 8. Data/model residuals look virtually identical to those in Model 8 and are not plotted. The width σ of the narrow Kα line, 66^{+19}_{-22} eV, corresponds to a FWHM velocity of 7000 km s^{-1}. For Keplerian motion, this corresponds to a radius of $\sim 900 R_{\rm Sch}$ ($1\ R_{\rm Sch}=2GM_{\rm BH}/c^2$).

Given that models with relativistic disklines (models 8, 9A, and 9B) provide a superior fit to the emission profile compared to the double-Gaussian models (4 and 5) or models with double-Gaussians plus a Compton shoulder, particularly in accounting for the presence of a Kα red wing, we can conclude that some sort of diskline is indeed required to best model the emission. However, a degeneracy in modeling the profile is apparent: models containing two broad lines and two narrow lines can be fit the observed profile of IC 4329a equally well using either a low-inclination diskline (plus little or no narrow emission) or by narrow components plus high-inclination disklines.

To further quantify the presence of emission features in the Fe K bandpass in addition to the Fe Kα and Kβ profiles, we added a narrow Gaussian to Model 8, and, using the STEPPAR command in XSPEC, derived confidence contours of line intensity versus rest-frame energy. We stepped through values of the energy centroid in the range 5.60–8.30 keV in increments of 0.05 keV and flux range 0–3×10^{-5} ph cm^{-2} s^{-1} in increments of 1×10^{-6} ph cm^{-2} s^{-1}. The width σ was kept fixed at 100 eV. The results are shown in the top panel of Figure 5, and demonstrate that there were no additional obvious signatures of emission, including those from the Fe XXV triplet or from Fe XXVI Lyα at their rest-frame energies. Similarly, adding an inverted Gaussian to quantify absorption, searching over the flux range 0 to -2.2×10^{-5} ph cm^{-2} s^{-1} showed that there was no strong evidence from these plots for strong resonance absorption at the rest-frame energies of Fe XXV or Fe XXVI (see Figure 5, bottom panel). The only strong narrow absorption feature was the 7.7 keV feature.

To further additional quantitative limits on K-shell Fe XXV and Fe XXVI emission and resonance absorption, we modified Model 8 by adding a narrow (σ = 65 eV) Gaussian (inverted for absorption). The energy centroid was fixed at 6.70 or 6.97 keV for He- or H-like Fe; though given the energy resolution of the pn, it would not have been possible to determine whether it was the forbidden, intercombination, or resonance line that was responsible for the He-like emission. In all cases, we found that adding a Gaussian increased χ^2, and found only upper limits to emission or absorption. The upper limits on the absolute values of the intensity (EW) for Fe XXV emission, Fe XXVI Lyα emission, Fe XXV absorption, or Fe XXVI Lyα absorption were 8.5×10^{-6} (8 eV), 13.2×10^{-6} (15 eV), 2.4×10^{-6} (3 eV), and 1.8×10^{-6} ph cm^{-2} s^{-1} (2 eV), respectively, consistent with the results of Bianchi et al. (2005) for the 10 ksec *XMM-Newton* observation of IC 4329a in 2001.

From our analysis, we conclude that the sets of models containing dual-disklines (8, 9A, or 9B) are equally adequate in fully describing the Fe K emission profile of IC 4329a, since there is no formal requirement for additional emission lines.

4.3. *The 7.68 keV narrow absorption feature*

We now turn our attention to modeling the narrow absorption feature which appears at ~7.7 keV. This feature cannot be attributed to relativistic diskline emission, and appears in the data/model residuals independently of how the Fe K emission lines are parameterized. We assume that it has a physical origin distinct from that of the emission lines. §4.3.1 discusses simple model fits to the absorption line. In §4.3.2, we show that this feature is likely not an artifact of the background, and in §4.3.3, we discuss the statistical significance of detecting this feature, and present the results of a Monte Carlo simulation analysis which show that the feature is almost certainly not due to photon noise. Based on these results, we can safely assume the feature is intrinsic to the source, and in §4.3.4, we discuss possible origins for the line.

4.3.1. *Gaussian model fit for the line*

We started with Model 8, the power-law + PEXRAV + double-diskline model (though the reader is reminded that Models 9A and 9B provide an equally acceptable fit to the emission profile, and the spectral-fit results for the absorption line are independent of which model is used to describe the emission profile). We first tested the hypothesis that the feature was indicative of reflection off ionized material. First, we substituted the PEXRAV component with a PEXRIV component (Model 10); an increase in the ionization level of the reflecting material pushes the energy of the Fe K absorption edge from 7.1 keV up towards higher energies. However, using a PEXRIV component, with disk temperature $T_{\rm disk}$ kept fixed at 30,000 K, resulted in a best fit virtually identical to Model 8. The value of the ionization parameter ξ (defined as $4\pi F_{\rm ion}/n$, with $F_{\rm ion}$ defined as the 0.5–20 keV ionizing continuum flux and n is the density of the reflecting material) was 0 erg cm s^{-1} (upper limit of 0.04 erg cm s^{-1}). χ^2/dof increased to 1838.46/1889 with no improvement in the data/model residuals. Forcing the Fe K edge energy to be near 7.4–7.7 keV by constraining ξ to be near ~3–10 erg cm s^{-1} did not successfully remove the residuals. Thawing $T_{\rm disk}$ provided no improvement to the fits. Models simultaneously incorporating PEXRAV and PEXRIV components, with absorption edges near 7.0 keV and 7.4–7.5 keV, respectively, also did not account for the 7.7 keV residuals. In all cases, an Fe K absorption edge near 7.1 keV, consistent with reflection off of neutral material, was still required by the data (see, e.g., Gondoin et al. 2001).

We tested the notion that the feature could be an absorption edge, independent from Compton reflection. We returned to Model 8 (with PEXRAV), and included an edge component (Model 11). The best-fit model was one with

an edge energy of $7.17^{+0.25}_{-0.17}$ keV and an optical depth τ of 0.03±0.01. However, the data/model residuals near 7.6 keV were not affected. Attempts to force the edge energy closer to 7.4–7.6 keV were also unsuccessful in removing the data/model residuals. Spectral parameters for the best fit Models 10 and 11 are listed in Table 7. From the results of the Model 10 and 11 fits, one can conclude that the feature is too narrow to be an absorption edge.

We then attempted to model the feature using a simple narrow, inverted Gaussian. We returned to Model 8, and added an inverted Gaussian near 7.7 keV (Model 12). The best-fit model successfully removed the data/model residuals, as shown in Figure 4. Spectral parameters for the best fit Model 12 are listed in Table 7. The best-fit rest-frame energy centroid was $7.68^{+0.04}_{-0.03}$ keV (corresponding to $7.56^{+0.04}_{-0.03}$ keV in the observed frame). The best fit width σ was 35^{+65}_{-35} eV. The absolute value of the intensity was 9.6±3.4 × 10^{-6} ph cm^{-2} s^{-1} for an $|EW|$ of 13±5 eV. The value of χ^2/dof was 1813.50/1887, the best-fit model so far. Compared to Model 8, χ^2 dropped by 21.73, and an F-test for adding this component yielded F=7.54, with a null hypothesis probability of 5.2×10^{-5}. However, as discussed in §4.2.3, there was no a priori reason to expect an absorption feature in this energy bandpass, and the F-test, when used in this "standard" manner, tends to overestimate the significance of detecting a feature. The statistical significance of detecting this component will be addressed in more detail in §4.2.3.

Finally, having properly quantified the emission and absorption profile, we investigated the Fe abundance by studying the height of the 7.1 keV edge relative to the Compton reflection strength. In the PEXRAV model, the Fe abundance had been kept frozen at 1.0, using the Anders & Grevesse (1989) tables. Keeping R frozen at 0.51 and thawing the Fe abundance made no change in the fit statistic; the best-fit Fe abundance was $1.0^{+1.0}_{-0.4}$. Using the Grevesse & Sauval (1998) tables, the best-fit Fe abundance was 1.5±0.7.

4.3.2. *PN background/instrumental effects*

The pn background spectrum shows no obvious features around observed-frame energies of 7.5–7.6 keV. However, two instrumental features, a Ni Kα emission line at 7.48 keV and a Cu Kα emission line at 8.05 keV, are expected (Katayama et al. 2004; Freyberg et al. 2004). These lines originate from the electronics board located below the CCD camera. However, there are no obvious features in pn background spectrum for IC 4329a at these energies (see Figure 6). One might initially suspect that the 7.56 keV (observed-frame) absorption feature could be an artifact resulting from the 7.48 keV instrumental line, but there are several arguments against this notion. First, the background count rate is a factor of ∼40 fainter than that of the source background: the 5–9 keV count rates in the background and source (after background subtraction) were 0.045 c s^{-1} and 1.748 c s^{-1}, respectively. Additionally, there were no differences seen in the data when screened against the periods of highest background rates, as discussed in §2. Second, if it were the case that the 7.48 keV line is relevant in affecting the spectrum, then one might also expect features near 8.05 keV as well, since the 8.05 keV line is actually stronger (Katayama et al. 2004); however, no such features are evident in the pn spectrum here. Third, these instrumental lines' fluxes are at a minimum within 5′ of the core (Katayama et al. 2004); the background in this case was extracted over a region located 3′ away from the core. Fourth, we note that S05 attempted to detect expected instrumental features in the pn background to verify the energy scale, but did not detect any instrumental lines with sufficient significance.

Our own attempts to model these features in the source spectrum also argue against the notion these features were somehow not properly subtracted. For simplicity, we started with Model 8, the dual-diskline model. A third Gaussian component was added, with energy fixed at either 7.48 keV or 8.05 keV. The Gaussian width σ was set to 1 eV initially, but allowed to vary. The line normalization was allowed to be positive or negative. The best fits still yielded significant residuals near 7.5–7.6 keV, and failed to achieve as good a model fit as Model 12. We are confident in concluding that the feature at 7.56 keV in the observed frame is intrinsic to the spectrum of IC 4329a and is not an artifact of the instrument or the background.

It has been reported that for pn "double event" data, events where photon energy is deposited on adjacent pixels, the registered photon energy can be 20 eV greater than the energy corresponding to an otherwise-identical single-pixel event (e.g., Pounds & Page 2005). The pn data had initially been extracted using pattern 0–4 events (single and double events); to test for this effect, we re-analyzed the pn data using only single-event (pattern=0) data. For both filtered and unfiltered data, the pattern=0 spectrum was virtually identical to the pattern≤4 spectrum, though with ∼30% fewer counts, and a continuum slope that was steeper by ∼0.05 in photon index. Importantly, however, the fitting results for Fe K bandpass features were virtually identical in all cases. We conclude that the emission and absorption features modeled here are not artifacts of pattern selection. The data/model continuum residuals showed slight improvement above ∼9 keV, but since our focus was quantifying the Fe K bandpass features using the maximum usable exposure, we continued to use the pattern≤4 data.

4.3.3. *Estimating the significance of the detection of the 7.68 keV absorption feature*

The standard, two-parameter F-test for the addition of a Gaussian to model the absorption line at 7.68 keV yielded a null hypothesis probability (the probability that the null hypothesis, that the model without an absorption line at 7.68 keV, is correct) of 5.2×10^{-5} (∼4.1σ significance). However, using the F-test in this manner has a tendency to overestimate the detection significance, as the F-test does not take into account the possible range of energies where a line might be expected to occur, nor does it take into account the number of bins (resolution elements) present over that energy range. The F-test can yield the probability P_1 (equal to one minus the null hypothesis probability) of finding a feature at a given energy *if the line energy is known in advance* (see e.g., warnings by Protassov et al. 2002). However, in this case, there was no a priori expectation of a 7.68 keV feature, and in searching for narrow features at arbitrary energies, one is searching over many resolution elements and needs to account for

the possibility that narrow features can occur by chance due to statistical noise. One might search the 4–9 keV bandpass for Fe K emission or absorption lines, including narrow features near 5–6 keV that have been generally interpreted as gravitationally redshifted Fe K emission (e.g., Turner et al. 2002, 2004). There are about 36 pn resolution elements over this energy range. The probability of detecting a feature at any energy in this range due is found from $(P_1)^N$, where N is the number of resolution elements. For IC 4329a, the probability that the 7.68 keV feature is spurious thus becomes 1.9×10^{-3}. This is still significant at greater than 3.1σ significance. It is noted that if the spectral bin sizes are smaller than the instrument resolution, then the number of bins where a line may be located has probably been over-estimated; this means the detection probability may have been underestimated.

Monte Carlo simulations were performed as an additional test of the line significance (see Porquet et al. 2005). These simulations tested the null hypothesis that the spectrum is well-fitted by a model that does not include the 7.68 keV absorption feature. For simplicity, Model 8 (a power-law plus a pexrav component, plus two disklines for Fe Kα and Fe β emission, all modified by WABS) was initially assumed. In order to generate 1000 fake spectra, with the photon statistics appropriate for a 93 ksec good time exposure, one could simply run the XSPEC command "fakeit" on this model 1000 times. However, this process does not account for the uncertainty in the null hypothesis model itself; such uncertainty is relevant, for example, when one is testing for the presence of broad features, when broad features are present in the null hypothesis model, or when the original data set is relatively noisy. Instead, we initially assumed the null hypothesis model, ran fakeit once, with the photon statistics for a 93 ksec exposure, and then re-fit the model to this new faked data set, yielding a "modified" null hypothesis model. We ran fakeit a second time, using this modified model, to generate a second faked spectrum. This entire process was repeated 1000 times to generate 1000 fake spectra (based on the range of the 1000 "modified" null hypothesis models, as opposed to the single, original model). For each faked spectrum, we fit a model of the same as the null hypothesis model, obtaining a χ^2 value (hereafter $\chi^2_{\rm null}$). We then added a narrow Gaussian component (width σ fixed at 10 eV) to the fit. The Gaussian normalization was allowed to be positive or negative, to account for the possibility of detecting either an emission or absorption feature (since there had been no a priori expectation to expect either). We searched over the energy ranges 4.0–6.1 keV and 7.1–10.0 keV. The range 6.1–7.1 keV was excluded to avoid the possibility that the e.g., Fe K emission lines or 7.1 keV PEXRAV edge would bias the Monte Carlo results. For each faked spectrum, we stepped the Gaussian centroid energy over these energies in increments of 0.1 keV (e.g., slightly higher than the instrument resolution), fitting separately each time to ensure that the lowest value of χ^2 was found. For each faked spectrum, the minimum value of χ^2 was compared with $\chi^2_{\rm null}$, yielding a $\Delta\chi^2$ value. Repeating this process 1000 times yielded a distribution of 1000 $\Delta\chi^2$ values which could then be compared with the observed $\Delta\chi^2$ value, which for this case was – 21.73. The result of these simulations was that a $|\Delta\chi^2|$ value of 21.73 was not exceeded even once. The values of $|\Delta\chi^2|$ corresponding to the 68, 90, 95, and 99.0% values in the cumulative frequency distribution were 6.8, 9.5, 11.1, and 14.4, respectively; the highest simulated $|\Delta\chi^2|$ value was 18.1. The simulations thus suggest that the probability that the null hypothesis model was correct is at most 1/1000, or that the 7.68 keV absorption feature is detected at >99.9% confidence.

Finally, we briefly address "publication bias": there are approximately a dozen *XMM-Newton* observations of Seyfert 1s of similar length and quality to the current observation. One could thus argue that the significance of detecting the 7.68 keV feature should be reduced to $\gtrsim$98.8%, given that there was no a priori reason to expect an absorption feature at such an arbitrary energy. We leave it to the reader to include the relevance of such publication bias. However, given the very high value of $|\Delta\chi^2|$, the unlikeliness that the feature is an artifact of background modeling, and and the low probability that this could be due to photon noise, we henceforth assume that the 7.68 keV absorption line is intrinsic to IC 4329a.

4.3.4. *The origin of the line*

As far as the origin of this feature is concerned, there are several candidates to consider. K-shell absorption due to Fe XXV or Fe XXVI is a prime candidate, given that other absorption lines attributed to highly-ionized Fe have been found in AGN. If the 7.68 keV line is due to Fe XXVI, then it is blueshifted by 0.72 keV, implying an origin in material that is blueshifted by nearly 31000 km s^{-1} relative to systemic. If the line is due instead to Fe XXV, then the blueshift is even higher: assuming an origin in the resonance line (6.697 keV in the rest-frame), then a blueshift of 0.98 keV relative to systemic is required, suggesting an origin in matter flowing $\sim$44000 km s^{-1} towards the observer and relative to systemic.

To shed additional light on the origin of this feature, we modified the double-Gaussian model to include absorption due to ionized material along the line of sight (Model 13). We modified Model 8 by including an XSTAR component, assuming solar abundances, and keeping the redshift as a free parameter. The best-fit model (see Table 7) was one with a high ionization parameter ξ: $\log(\xi) = 3.73^{+0.15}_{-0.13}$ erg cm s^{-1}. χ^2/dof was 1809.17/1887, a slightly better fit compared to Model 12. The column density required was $1.4^{+1.0}_{-0.5} \times 10^{22}$ cm^{-2}, and the required radial velocity shift relative to systemic was $-0.093^{+0.006}_{-0.002}c$, or $\sim -27000^{+2000}_{-1000}$ km s^{-1}. At this ionization level, the expected dominant absorption line, and the most likely origin of this feature, is due to Fe XXVI. The best fit model is thus consistent with the interpretation above that the absorption feature has an origin in highly-ionized material outflowing at $\sim 0.1c$ relative to systemic.

It is unlikely that the absorption feature is due to Kβ absorption by highly-ionized Fe (greater than F XVII), otherwise one would expect strong Kα absorption by the same species. For example, if the 7.68 keV absorption feature is due to redshifted Fe Kβ XXV, with a rest frame energy near 7.87 keV, this implies a redshift of 0.024 relative to systemic. If the material which gives rise to this feature has an ionization parameter ξ of $\sim$3.2–3.7, then we would expect very strong Fe Kα XXVI and Fe Kα XXV res-

onant absorption at the same redshift, appearing at rest frame energies of 6.80 and 6.51 keV, respectively. Looking at the residuals in Models 12 or 13, there are no obvious residuals at these energies. Adding an inverted Gaussian with centroid energies fixed at either location, and width fixed at 35 eV (the Gaussian width of the 7.68 keV line in Model 12), results in no improvement to the fit, with upper limits to the equivalent widths of 3 eV in either case. If the 7.68 keV feature is due to redshifted Fe Kβ XXVI (rest frame energy near 8.3 keV), the implied redshift relative to systemic is 0.075, causing the Fe Kα XXVI and Fe Kα XXV lines to appear at rest frame energies of 6.48 keV and 6.20 keV, respectively. The upper limits to absorption at these energies are 3 eV and 8 eV, respectively, with no fit improvement in either case.

Similarly, it is unlikely that the 7.68 keV feature is due to blueshifted Kβ absorption from lowly-ionized Fe ($\sim$7.1–7.2 keV rest frame). The absorbing gas would have to have an ionization parameter smaller than log$\xi \sim 2.1$ in order for absorption near $\sim$7.1–7.2 keV to exist. For an absorber with logξ=2.0 and a blueshift of 0.07c, a column density of 1.1×10^{22} cm^{-2} is required to fit the 7.68 keV absorption line. However, this model requires very strong spectral curvature below $\sim$4 keV; such curvature is not seen in the EPIC spectrum, as XSTAR modeling using low ionization photo-ionized absorbers yield poor fits to the pn spectrum below $\sim$4 keV for column densities above roughly 10^{21} cm^{-2}. Additionally, for photoionized material in the approximate range logξ = 1.5–2.1, Fe Kα absorption is just as strong, or stronger than, the Fe Kβ absorption. For material in this range of ionization parameter, if the 7.68 keV line were due to neutral or lowly-ionized Fe Kβ absorption, blueshifted by $\sim$0.6, then we would expect neutral Fe Kα absorption to appear near 6.9 keV (rest frame). There are no obvious residuals near this energy in Models 12 or 13. Forcing an inverted Gaussian into the model, with width tied to that for the 7.68 keV Gaussian line, yields no change in the fit, with limits to the absolute values of the intensity and equivalent width of 2.7×10^{-6} ph cm^{-2} s^{-1} and 2.8 eV, respectively. One can alleviate the requirement of having Fe Kα absorption by noting that Fe Kα is negligible compared to Fe Kβ for very low values of the ionization parameter (log$\xi \lesssim 1.2$). For these ionization parameters, the dominant species will be <XVII; the L-shell is full, so Kα absorption cannot be produced. However, as above, the required column density in this case would introduce very strong spectral curvature into the spectrum at and below $\sim$4 keV, which is not seen. An origin for the 7.68 keV absorption feature in Fe Kβ thus seems unlikely.

We next considered the possibility that the 7.68 keV absorption feature could be due to very highly-blueshifted, moderately-ionized Fe Kα (Fe XVII–XXII or so, with rest-frame energies near 6.44–6.51 keV). For instance, an XSTAR absorber with logξ=2.1$\pm$0.2, a column density $N_{\rm H}$ = 1.8$\pm$0.5 $\times10^{20}$ cm^{-2}, blueshifted by 0.16 $\pm$0.01 c relative to systemic provides almost as good a fit above 3 keV as Model 13, with χ^2/dof = 1820.49/1887 for the best-fit model. Because moderately-ionized Fe has a higher opacity than H- or He-like Fe, a lower column density can account for the 7.68 keV absorption line without intoducing strong spectral curvature around 3–4 keV. However, extrapolation of this model to energies down to $\sim$0.9 keV reveals large data/model discrepancies. Specifically, for a logξ=2.1 absorber with $N_{\rm H} \sim 2\times10^{20}$ cm^{-2}, one expects very strong (EW = 25–30 eV) absorption features near rest-frame energies of $\sim$0.91–0.94 keV due to L-shell absorption by moderately-ionized Fe $\sim$ XIX–XX and near 1.86 keV, likely due to absorption in He-like Si. For an absorber blueshifted by 0.16c, we would expect such features to appear at 1.06 and 2.13 keV. However, the pn data at those energies show no such features; upper limits to inverted Gaussians fixed at those energies yield only small (< 1 eV) upper limits. An origin in very highly blueshifted Fe XVII thus seems unlikely.

There are transitions around 7.6–7.8 keV associated with highly ionized Ni K (XXV – XXVI or so), but an origin in Ni K at a velocity shift that is close to or at systemic seems unlikely: unless Ni is many times overabundant compared to Fe in IC 4329a, we would expect to see very strong evidence of additional absorption due to highly-ionized Fe Kα in the $\sim$6.6–6.96 keV range. Even if the 7.68 keV feature is due to strongly redshifted He- or He-like Ni or strongly blueshifted low- or intermediate-ionized Ni, we would still expect strong evidence for additional Fe K absorption lines at the appropriate redshift or blueshift. Given that there is only one absorption line strongly evident in the data, an origin in Ni seems unlikely.

A local (z=0) origin should be discussed as well, given that several recent soft X-ray AGN spectra have revealed evidence for absorption due to the local hot interstellar medium (e.g., McKernan, Yaqoob & Reynolds 2004). In the case of IC 4329a, for this line to be local in origin, it would have to originate in Kβ absorption from intermediate ionized Fe (Fe $\sim$ XXII). However, the very high column density required to produce such a line ($\gtrsim10^{22}$ cm^{-2}) is an implausible physical description of the local hot interstellar medium. Similarly, the relativistic velocities required for strongly blueshifted Fe Kα absorption are not associated with the local hot interstellar medium, and a local origin for the line is unlikely.

Finally, Figure 7 shows a model spectrum of the effect of the soft X-ray absorbing components seen in S05 on a simple power-law continuum. These low and moderately ionized components are too low in column density to introduce strong spectral curvature above $\sim$4 keV, suggesting that our emission and absorption modeling of the Fe K bandpass is robust.

4.4. *Consistency checks*

We checked for consistency between the pn and the MOS2 by applying the above models to the MOS2 data. We ignored all MOS2 data below 4.5 keV due to calibration uncertainties and data above 12 keV. Figure 8 shows the pn and MOS2 residuals to models consisting of a power-law plus PEXRAV, modified by neutral absorption; the shape of the Fe K profiles are overall similar. Applying the models above to the MOS2 data yielded similar and statistically acceptable fits. That is, most spectral parameters were consistent between the two instruments, though the photon indices for the MOS2 spectra were about 0.15 steeper. We were able to confirm that the Fe Kβ line is detected in the MOS2 data at $\sim$90% confidence, using an F-test to compare models 3 and 4. However, due to the lower sig-

nal/noise in the MOS2, it was not possible to verify e.g., the existence of the 7.68 keV absorption line or confirm that a dual-diskline model was a better fit than a double-Gaussian model.

To check for consistency between the pn and the *RXTE* PCA, we generated a '7-day' simultaneous PCA spectrum using *RXTE* data taken from the 36 obsids which occurred within ±3.5 days of the midpoint of the *XMM-Newton* observation. This resulted in a PCA spectrum with a good exposure time of 19.6 ksec, enough to confirm that an Fe Kα line is present, but not enough to detect other Fe K bandpass spectral features. The photon index for Model 3, applied to the '7-day' spectrum, was 1.89±0.4, steeper than that of the model when applied to the pn data. The 2–10 keV flux from the '7-day', medium-term and long-term modeled spectra are 11.0×10^{-11} erg cm^{-2} s^{-1}, 11.2×10^{-11} erg cm^{-2} s^{-1}, and 12.0×10^{-11} erg cm^{-2} s^{-1}, respectively. These values are about 30% than the 2–10 keV flux estimated from model fits to the *XMM-Newton* pn spectrum, 8.9×10^{-11} erg cm^{-2} s^{-1}. This discrepancy with the PCA normalization has been noted previously; see e.g., Yaqoob et al. (2003) [3].

5. TIME-RESOLVED SPECTRAL FITTING

Studying the time-resolved variability of the Fe K line and continuum components provides a complementary analysis to single-epoch spectral fitting. The simplest models predict that if the reprocessing time scale is negligible, then variations in the Fe K line flux should track continuum variations, modified only by a time delay equal to the light travel time between the X-ray continuum source and the Fe K line origin. However, recent studies of both broad and narrow Fe K lines have not been able to support this picture (e.g., Iwasawa et al. 1996, 1999; Reynolds et al. 2000; Vaughan & Edelson 2001, Markowitz, Edelson & Vaughan 2003). Most of these studies found that Fe K lines tend to vary much less than the continuum, with no evidence for correlated variability, on any time scale. Markowitz, Edelson & Vaughan (2003) additionally showed that Fe K lines, like the continuum, tend to exhibit stronger variability amplitudes towards relatively longer time scales.

Variability of narrow absorption features has also been reported, e.g., Reeves et al. (2004) found evidence for the narrow Fe XXV absorption line in the *XMM-Newton* spectrum of NGC 3783 to increase in equivalent width over ∼a day, suggesting an origin close to the central X-ray illuminating source. We investigated time-resolved spectroscopy IC 4329a to search for changes in the profile, fluxes, or peak energy of the Fe K emission or 7.68 keV absorption features in IC 4329a, and explore if any such variations are linked to continuum flux variations.

We started with short-term data and split the pn data into two time halves, each covering a duration of 66.3 ksec and with a good time exposure of 46.4 ksec. We fit each spectrum over 2.5–12 keV with Model 12 (dual-diskline plus narrow Gaussian in absorption). The best-fit spectral parameters, listed in Table 8, are all consistent with each other; differences in best-fit values can likely be attributed to less-than-optimal photon statistics. There is no evidence for temporal evolution in any of the absorption and emission profile parameters. The data/model residuals when each spectrum is fitted with a simple absorbed power-law are plotted in Figure 9 and show no obvious changes in the profile. However, given that the hard X-ray continuum light curve (shown in S05) displays minimal variability on these time scales, this is not surprising. Additionally, given the minimal continuum variability, we did not investigate spectral variability as a function of flux, i.e., high/low-flux states.

Next, we performed high time-resolution spectroscopy on all time scales to yield light curves of Γ and the Fe K flux. Time bins were chosen with the goals of achieving adequate signal-to-noise in the Fe K flux light curve. The medium-term data were divided into 18 bins, each covering a duration of 1.972 days, or once every 30 satellite orbits; each bin contained ∼10 separate *RXTE* visits. The average exposure time per bin was 5.6 ksec. The long-term data were divided into 18 bins of approximately 44 days each in duration, with no bin overlapping the two 56-day monitoring gaps: data from the periods 2003 Apr 08 – 2003 Sep 29, 2003 Nov 24 – 2004 Sep 30, and 2004 Nov 25 – 2005 Oct 02 were divided into 4, 7, and 7 bins, respectively. The average good time per bin was 8.1 ksec, excluding bins 3 (100.9 ksec) and 4 (68.7 ksec), which overlapped with the medium-term sampling.

Models were applied to time-resolved data based on the time-averaged fits. The short-term data were divided into 8 time bins, with each bin covering a duration of 16.6 ksec a with a good time exposure of 11.6 ksec. Spectral fitting was done over 2.5–12 keV. Model 5 (see Table 2), which featured Gaussians for the Fe Kα and Kβ emission lines, was used for the short-term spectra. Using the dual-diskline model offered no improvement to the fits; also, the 7.68 keV absorption line was not detected in any time-resolved spectrum. For both the long- and medium-term data, Model 3 (see Table 1), which featured a single Gaussian to model the Fe Kα emission, was used. More detailed fits were not practical, e.g., the Fe Kβ line was not detected. Spectral fitting was done over 3.5–24 keV. The HEXTE statistical errors were too large to study variability, so HEXTE was excluded from the time-resolved analysis. The Fe K α line detected in nearly every time bin at 99.8% confidence or greater in an F-test. When fitting the time-average models, it was not practical to thaw parameters such as the Fe K line profile shape or peak energy, given the PCA resolution and sensitivity. The neutral absorbing column density was kept as a free parameter. The F-test was used to determine which free parameters to include in the fits. The time-resolved spectral fits were repeated with each of photon index Γ, reflection fraction R, and Fe Kα line normalization $I_{\rm Fe}$ frozen at their time-averaged values, and the values of total χ^2 were compared via an F-test to determine which parameters could justifiably allowed to be free in the fits. The results are shown in Table 9. We found no formal requirement to thaw R on any time scale: the total values of χ^2 decreased only by 0.06 or 0.01 (long and medium, respectively) when R was thawed from the time-averaged value. All analysis hereafter assumes R is kept fixed at the time-averaged value for each time scale. As shown in Table 9, it was significant at >99.99 confidence to thaw Γ only on the medium and

[3] This issue is also discussed in an *ASCA* Guest Observer Facility Calibration memo at http://heasarc.gsfc.nasa.gov/docs/asca/calibration/3c273_results

long time scales, suggesting statistically significant variations in Γ on these time scales. It was significant at >99% confidence to thaw $I_{\rm Fe}$ only on the long time scale. Errors on the Fe K line flux and Γ light curves were determined using the point-to-point variance, as discussed in detail by Vaughan & Edelson (2001) and Markowitz, Edelson & Vaughan (2003). The 2–10 keV flux F_{2-10} was measured from each model fit. Errors on F_{2-10} within a time bin were derived from the 2–10 keV continuum light curves, using the distribution of points within that time bin.

Mean spectral fit values and errors are listed in Table 10. Figure 10 shows the light curves for F_{2-10}, Γ, and $I_{\rm Fe}$ for all three time scales We note that the long-term averages to the spectral fit parameters shown in Figure 10 and listed in Table 10 do precisely match the spectral-fit parameters to the long-term time average-spectrum listed in Table 1. (see §4.4 for notes comparing the PCA and pn 2–10 keV relative flux normalizations). This is due to the fact that the long-term time-average PCA spectrum has a substantial contribution from the medium-term time-average spectrum (the medium-term time-average spectrum comprises 36% of the long-term spectrum's total exposure time). Figure 11 shows correlation diagrams for Γ and $I_{\rm Fe}$ plotted against F_{2-10}. Table 10 also lists the Pearson correlation coefficients and null hypothesis probabilities. Finally, the fractional variability amplitudes, $F_{\rm var}$, as defined in Vaughan et al. (2003), are listed in Table 11 for the light curves.

From Figures 10 and 11 and Tables 10 and 11, one can see that there is not much variability in F_{2-10} or Γ on short time scales. However, Γ tends to correlate well with F_{2-10} on all three time scales, despite the somewhat narrow range spanned by F_{2-10}. However, there is no strong evidence for variability in $I_{\rm Fe}$ on any time scale; null hypothesis probabilities for a constant line flux cannot be rejected at greater than 60% confidence on any time scale. The lack of variability of the Fe line flux on short time scales has already been reported by S05. The results on long time scales are similar to those of Weaver, Gelbord & Yaqoob (2001), whose did not find any evidence for strong Fe line flux variability in IC 4329a based on five separate *ASCA* observations between 1993 and 1997.

6. DISCUSSION

6.1. *The Fe K emission profile: moderately-relativistic disklines*

The *XMM-Newton* pn spectrum of IC 4329a reveals an Fe K emission profile with two peaks, identified as Fe Kα at 6.4 keV and Fe Kβ at 7.0 peak. The 6.4 keV peak is much stronger in terms of both *EW* and height above the power-law continuum than the 7.0 keV peak, ruling out models wherein both peaks are the Doppler horns of a single relativistic diskline model (e.g., McKernan & Yaqoob 2004). The red peak in particular is not symmetric: a moderate red wing is present, and models incorporating two symmetric peaks do not provide as good a fit to the data as models incorporating at least moderately-relativistic diskline emission from Fe Kα and Fe Kβ. IC 4329a's Fe K emission profile is thus distinct from more symmetric and more narrow profiles which lack a red wing, such as that seen in NGC 5548 (Yaqoob et al. 2001, Yaqoob & Padmanabhan 2004). Such narrow, symmetric profiles are generally suspected of having an origin in matter far from the black hole, such as in the outer accretion disk, broad line region, or the molecular torus. In IC 4329a, however, the presence of a moderate red wing leads us to conclude that the emission profile is instead modeled equally well with either of the following two scenarios: 1) each peak is modeled by a low-inclination, moderately-broadened diskline, plus little or no contribution from a narrow emission line, or 2) each peak is modeled as the sum of a narrow line, to account for the emission closest to the rest energy of the line, plus a high-inclination diskline. In the latter case, neither the narrow nor broad component dominates the emission.

In some Seyferts, identification of broad Fe lines is complicated by model degeneracies which arise when 3–6 keV spectral curvature due to warm absorption is taken into account (e.g., Reeves et al. 2004, Turner et al. 2005). In IC'4329a, however, only minimal spectral curvature above 3 keV, and no spectral curvature above 5 keV, is expected given the results of soft X-ray absorption modeling (see Figure 7), and so the detection of a moderate red wing is robust. The best fitting model includes emission extending in to a radius of $13^{+13}_{-11.8}$ $R_{\rm g}$, similar to that found by Done et al. (2000) using *ASCA*. Done et al. (2000) note that IC 4329a's profile does not seem as broadened and reddened as that of MCG–6-30-15, where the diskline emission extends down to a $\sim$2–3$R_{\rm g}$ (Wilms et al. 2001; Young et al. 2005). The red wing emission in IC 4329a extends down to energies of $\sim$5.4 keV (Done et al. 2000) or $\sim$5.7 keV (this work), as opposed to energies below 4–5 keV in the case of MCG–6-30-15. Although our analysis cannot formally rule out an inner emission radius of $\lesssim 2R_{\rm g}$, the Fe K emission profile in IC 4329a thus seems to fall into a category between those consisting of narrow lines and those consisting of very strongly relativistically broadened lines.

Assuming that the bulk of the Fe K emission originates in the inner regions of an optically-thick, geometrically-thin accretion disk, as in case 1) above, these findings are consistent with the notion that the accretion disk in IC 4329a could be truncated below $\sim$10–20 $R_{\rm g}$, or could transition from a geometrically-thin, optically-thick disk at large radii to a radiatively-inefficient flow, such as an advection-dominated accretion flow (ADAF; Narayan & Yi 1995), in the innermost regions of the accretion disk, e.g., Dove et al. (1997) and Esin, McClintock & Narayan (1997).

Additionally, for case 1), the best-fit rest energy for the Fe Kα diskline was 6.44$\pm$0.01 keV, more consistent with an origin in moderately-ionized Fe than in neutral Fe; the likely dominant ionization stage is $\sim$XVII. This phenomenon could be related to IC 4329a's high X-ray luminosity. Using the *XMM-Newton* 2–10 keV flux of 9×10^{-11} erg cm^{-2} s^{-1}, we derive an 2–10 keV luminosity L_{2-10} of 5.1×10^{43} erg s^{-1} (assuming $H_{\rm o}$=70 km s^{-1} Mpc^{-1} and $\Lambda_{\rm o}$=0.73). Similarly, Yaqoob & Padmanabhan (2004) measured Fe line energies that seemed more consistent with moderately-ionized Fe than neutral Fe in two other high-luminosity Seyferts, 3C 120 and Mkn 509.

The lack of variability in the Fe K emission line is consistent with an origin in distant matter, as suggested e.g., by S05. However, the line profile suggests a non-negligible contribution from material origin close to the black hole.

If in fact the bulk of the Fe K emission originates in the inner accretion disk, as in case 1), then a likely scenario is as follows: assuming that variations in the line track those in the X-ray continuum, modified only by a light travel time delay, the line will not vary strongly unless the continuum does. However, the continuum in IC 4329a does not display strong variability. Even on time scales of ~2 years, the peak-to-trough continuum variations do not exceed ~50%, which simply may not be sufficient to trigger very strong trends in Fe K flux. Similarly, with time bins chosen to maximize the variability-to-noise in the in the Fe flux light curves, this analysis may simply not be sufficiently sensitive to track small-amplitude trends (<50% variations) in line flux.

If there are approximately equal broad and narrow component contributions to the profile, as in case 2), then, for time scales longer than the light-crossing times between the continuum source and the sites of broad and narrow line production, it could again be the case that the lack of variability in either component is a result of the lack of strong continuum variability. However, the PCA is not sensitive enough to distinguish between the broad and narrow components. Therefore, if the narrow component, which comprises ~60% of the total (narrow plus broad) is constant, then the PCA time-resolved spectroscopy may not be sensitive to small changes in the broad component only on time scales longer than a few days. In any case, the lack of strongly-correlated variations between the continuum and line prevents us from making any firms conclusions about using variability to determine the location of the line-emitting material.

6.2. *The 7.68 keV absorption feature: the highly-ionized outflow in IC 4329a*

High-resolution spectroscopy of the Fe K band of several AGN has yielded evidence for highly-ionized absorbing gas, e.g., NGC 3783 (Reeves et al. 2004) and MCG–6-30-15 (Young et al. 2005). In addition, there is evidence in PG and BAL quasars for Fe K lines and/or edges which suggest absorbing gas which is both highly-ionized and outflowing at relativistic velocities. For instance, in PG 1211+143 (Pounds et al. 2003a), PG 0844+349 (Pounds et al. 2003b), PDS 456 (Reeves et al.2003), and the BAL quasars APM 08279+5255 (Chartas et al. 2002; Hasinger, Schartel & Komossa 2002), and PG 1115+080 (Chartas et al. 2003), the ionization parameters were typically $\log\xi \sim 2.5 - 3.7$, the outflow velocities spanned 0.08–0.34c, and the absorber column densities were typically ~1–5×10^{23} cm^{-2}. (although see McKernan, Yaqoob & Reynolds 2004 regarding caveats for PDS 456 and PG 1211+143).

The highly-ionized, high-velocity absorbing material in IC 4329a has a derived ionization parameter and outflow velocity similar to what is found in these objects, though we note that the derived column density for the IC 4329a's outflow component is about a factor of ten lower. Nonetheless, we hereby add IC 4329a to this rather small but growing list, noting that IC 4329a is thus the lowest-redshift AGN known to exhibit this type of outflow.

To estimate the distance r between the central black hole and the outflowing gas, we can use $\xi = L_{2-200} / (n\ r^2)$, where n is the number density. L_{2-200} is the luminosity corresponding to the 2–200 keV illuminating continuum, which we use instead of the 1–1000 Rydberg ionizing continuum luminosity because most of the photons that ionize this particular component are expected to be hard, not soft, X-rays. We estimate the maximum possible distance to the material by assuming that the the thickness Δr must be less than less than the distance r. Noting that the column density $N_{\rm H} = n\Delta r$ yields the upper limit $r < L_{2-200}/(N_{\rm H}\xi)$. We estimate the 2–200 keV flux from our models to be 4.9×10^{-10} erg cm^{-2} s^{-1}, which corresponds to L_{2-200} = 2.8×10^{44} erg s^{-1}. This yields $r < 3.8\times10^{18}$ cm, or 1.2 pc.

In the foremention PG and BAL quasars, the derived mass outflow rates are usually at least 1 M$_\odot$ yr^{-1} and on the order of the accretion inflow rate, suggesting that these outflows account for a substantial portion of the total energy budget of the AGN. Under the assumption that the gas is in equilibrium and that the outflow velocity is a constant, the mass outflow rate $\dot{M}_{\rm out}$ for the IC 4329a component can be derived via conservation of mass: $\dot{M}_{\rm out} = \Omega n r^2 v m_{\rm p}$, where v is the outflow velocity, $m_{\rm p}$ is the proton mass, and Ω is the covering fraction, which we will assume is $4\pi/10$ sr. Substituting $nr^2 = L_{2-200}/\xi$, we find an outflow rate of ~ 3×10^{27} gm s^{-1} = 5 M$_\odot$ yr^{-1}. We note that the actual outflow rate should be lower if there is an extreme degree of collimation, or higher if the outflowing component is not directed along the line of sight.

We can compare this to the inflow accretion rate $\dot{M}_{\rm acc}$ using $L_{\rm bol} = \eta\dot{M}_{\rm acc}c^2$, where η is the accretion efficiency parameter, typically 0.1. Using the relation of Padovani & Rafanelli (1988), $L_{\rm bol} = 59\nu L_\nu$ at ν=2 keV, and a photon index Γ of 1.75, the bolometric luminosity is thus estimated to be $L_{\rm bol} = 32L_{2-10} = 1.6\times10^{45}$ erg s^{-1}. We find $\dot{M}_{\rm acc} \sim 0.3$ M$_\odot$ yr^{-1}. The kinetic power associated with the outflow component, estimated as $\dot{M}_{\rm out}v^2$, is 3×10^{45} erg s^{-1}, a factor of ~60 higher than the bolometric luminosity. Similar to the situation in the aforementioned quasars, the outflow rate of this particular absorbing component may therefore represent a substantial fraction of the accretion inflow used to power the bolometric luminosity in IC 4329a. Similar calculations on the low-velocity, soft X-ray absorbing components (S05), using $L_{\rm ion}$, estimated to be 1.4×10^{44} erg s^{-1}, suggest that they, too, are associated with outflow rates that are of the same magnitude or higher than the inflow accretion rate.

The high-velocities of these outflows suggests that the outflow is likely to be associated with the accretion disk at a small radius. An explanation commonly invoked for the high-velocity, high-ionization absorbers in that the flow originates in the innermost part of a radiatively-driven accretion disk wind (e.g., Proga, Stone & Kallman 2002; King & Pounds 2003). In this scenario, the winds must be launched from very close in to the black hole, yet far enough away from the black hole that the outflow velocity exceeds the local escape velocity. For a Keplerian disk, the radius at which the escape velocity is 0.1c will be equal to $(v_{\rm esc}/c)^2 R_{\rm Sch} = 100R_{\rm Sch}$; a radiatively-driven wind could thus be applicable to IC 4329a if (neglecting acceleration) the wind is launched from a larger radius.

More specifically, King & Pounds (2003; see also Reeves et al. 2003) demonstrated that objects accreting near the Eddington rate are likely to exhibit radiatively-driven winds with substantial column densities, and the outflow

rates of these winds may be comparable to the accretion inflow rate. If the flow becomes optically-thick at small radii ($\sim$10–100 R_g), extreme velocities and high column densities are likely to the associated with the flow. This scenario may be applicable to the high-velocity absorber in IC 4329a. However, we do not know a priori if the accretion rate of IC 4329a is indeed near Eddington. Uncertainty regarding IC 4329a's black hole mass M_{BH} prevents precise knowledge about the accretion rate. The reverberation-mapped estimate for M_{BH} (Peterson et al. 2004) is formally an upper limit only, $9.9^{+17.9}_{-9.9}$ $M_\odot$, implying an accretion rate relative to Eddington of L_{bol}/L_{Edd} of $1.29^{+inf}_{-0.83}$. Other methods yield higher black hole mass estimates. For example, using the photo-ionization method (estimating velocity dispersions based on Hβ line widths) to estimate the distance from the central illuminating source to the broad-line region, Wandel, Peterson & Malkan (1999) estimate a black hole mass of 2.2×10^7 $M_\odot$. Along another track, Nikolajuk, Papadakis & Czerny (2004) suggest a prescription to estimate M_{BH} based on short-term X-ray variability amplitude measurement, specifically the normalized excess variance, σ_{NXS}. They estimate $M_{BH} = 1.24\times10^8$ $M_\odot$ based on short-term *RXTE* light curves. We rebinned the short-term, pn 2.5–12 keV light curve with a sampling time of 6.8 ksec, to yield a light curve with enough data points (20) to get an accurate measurement of σ_{NXS}. We found $\sigma_{NXS}= 0.00136 \pm 0.00010$ (errors derived using Vaughan et al. 2003); the Nikolajuk et al. (2004) relation yields a M_{BH} estimate of $8.64\pm0.60 \times 10^7$ $M_\odot$, similar to the Nikolajuk et al. (2004) estimate[4]. This value of the black hole mass places the estimated accretion rate L_{bol}/L_{Edd} at 15$\pm$1%. A more accurate black hole mass determination, e.g., via more accurate reverberation mapping, is needed to resolve this issue. We can only conclude that we currently cannot rule out an accretion rate close to the Eddington limit, and so a radiatively-driven disk wind cannot be ruled out.

Another problem with the disk-wind scenario is that the 7.68 keV absorption feature is narrow, and consistent with a single component only. A broad range of velocities seems more physically plausible if we are seeing a continuous stream of gas being accelerated from rest to 0.1c (relative to the systemic velocity). However, there are no such indications in the Fe K bandpass of material at lower velocities. These facts could suggest that we are witnessing a discrete, transient, outflowing 'blob' of material as opposed, to a continuous flow. In this case, the average mass outflow rate will be lower than the estimate given above, depending on the duty cycle of ejection.

In addition to radiatively-driven outflows, another mechanism whereby radio-quiet AGN can have material outflowing at relativistic velocities is described by the so-called "aborted-jet model" of Ghisellini, Haardt & Matt (2004). In this model, radio-quiet accreting black holes launch jets only intermittently, yielding discrete, fast-moving blobs that travel along the black hole rotation axis, as opposed to a jet that is continuously on. Extraction of black hole rotational energy, in addition to accretion energy, provides the energy source. The jet is launched at a velocity less the escape velocity, so blobs reach a maximum radius from the black hole before falling backwards and colliding with later-produced outflowing blobs. In the case of IC 4329a, we could thus be witnessing a singular, transient blob at a particular point in its outward journey, although its location must be < 100 R_{Sch} for this scenario to apply.

However, even if the gas is in the form of a discrete blob, this particular model may not be relevant. We cannot ascertain whether or not the material lies on the jet axis, and, due to uncertainty regarding the location of the material, it is difficult to ascertain whether the escape velocity exceeds the material's outflow velocity. Finally, the Fe K bandpass spectrum of IC 4329a yields no evidence for other discrete, absorbing blobs at any other velocity. Similarly, there are no indications from the soft X-rays (e.g., S05) for absorption at a similar relativistic outflow velocity, so the absorbing material would have to be in the form of a single blob consisting of a high-ionization component only, with no lowly- or moderately-ionized contribution, for such a scenario to be applicable.

Finally, we note that this high-velocity hard X-ray absorber is unlikely to be directly physically connected to the soft X-ray absorbers seen by S05. The soft X-ray absorbers are likely too low in outflow velocity, column density and ionization state to be part of the same outflow phenomenon as the hard X-ray absorber, suggesting physically distinct phenomena. There is no evidence that the soft X-ray absorbing material "feeds" or is "fed by" the hard X-ray absorber, and no obvious acceleration/deceleration mechanism.

7. CONCLUSIONS

We have presented a re-analysis of the *XMM-Newton* pn long-look spectrum of IC 4329a. The Fe K bandpass is dominated by two peaks, identified as Fe Kα and Kβ emission. The 6.4 keV peak is much higher in equivalent width and height above the continuum compared to the 7.0 keV peak, ruling out models whereby both peaks are the Doppler horns of a single relativistic diskline. Models featuring dual diskline components provide a better fit than a simple dual-Gaussian model, and demonstrate the necessity of including diskline components in emission models. However, there is a degeneracy present, in that the emission profile can be described equally well by either a model in which low-inclination dual-diskline profiles dominate the peaks, with little or no contribution from a narrow component, or a model in which approximately equal contributions from a high-inclination diskline and a narrow component describe each peak. The resolution of an X-ray calorimeter is needed to break the degeneracy between these two cases and deconvolve the narrow and broad components. There is no strong evidence for emission or absorption at the systemic velocity by Fe XXV or Fe XXVI; there is no strong evidence for a Compton shoul-

[4] We note that the Nikolajuk et al. (2004) method assumes that the power spectral density function (PSD) contains a 'break' (change in power-law slope from –2 to –1) at temporal frequencies corresponding to time scales larger than the duration over which one is measuring σ_{NXS} (see Nikolajuk et al. 2004 for derivation, as well as additional assumptions and caveats). PDS measurement for IC 4329a is still in progress, pending accumulation of long-term monitoring data, (Markowitz et al., in prep.), but we will assume that the PSD break for IC 4329a corresponds a time scale longer than 1.5 days (as expected for an AGN with a black hole mass larger than 5×10^6 $M_\odot$; see Markowitz et al. 2003).

der. In addition, we have used *RXTE* monitoring data to extract a PCA + HEXTE spectrum to derive tight constraints on the strength of the reflection component.

We have performed time-resolved spectral fitting on the *XMM-Newton* long-look and the *RXTE* monitoring data to probe the variability of the X-ray continuum, photon index and Fe K line flux on timescales spanning $\lesssim$a day to 2 years. The photon index and 2–10 keV flux are well-correlated. However, there is no strong evidence for variability in the Fe K line on any time scale probed, likely due to the minimal level of continuum variability.

We find strong evidence for a narrow absorption line at 7.68 keV. Monte Carlo simulations are used to verify the high level of detection significance. The most likely origin for the line is Fe XXVI, in highly-ionized material blueshifted by $\sim 0.1c$ relative to systemic. This phenomenon is similar to what is seen in other high luminosity AGN, including PG and BAL quasars, making IC 4329a the lowest redshift AGN known to exhibit this phenomenon. The mass outflow rate of this component is estimated to be larger than the inflow accretion rate, suggesting that the outflow represents at least a substantial portion of the overall energy budget. The outflow may be associated with a radiatively-driven disk wind. However, because of the narrow velocity range seen, it is also possible that the absorbing material is in the form of a discrete 'blob' of emission. It is important to find as many of these absorbing features as possible, to guage the frequency of occurrence in Seyfert AGN.

The authors thank Katrien Steenbrugge for insightful comments and suggestions, for providing the model used to make Figure 7, and for providing early access to EPIC proprietary data. The authors thank Philip Uttley for providing his Monte Carlo spectral simulation code. A.M. thanks Nikolai Shaposhnikov, Jean Swank and Craig Markwardt for guidance on HEXTE data reduction and spectral analysis. This work has made use of observations obtained with *XMM-Newton*, an ESA science mission with instruments and contributions directly funded by ESA member states and the US (NASA). This work has made use of data obtained through the High Energy Astrophysics Science Archive Research Center Online Service, provided by the NASA Goddard Space Flight Center, and the NASA/IPAC Extragalactic Database which is operated by the Jet Propulsion Laboratory, California Institute of Technology, under contract with the National Aeronautics and Space Administration.

REFERENCES

Anders, E. & Grevesse, N. 1989, Geochimica et Cosmochimica Acta, 53, 197
Arnaud, K. 1996, in *Astronomical Data Analysis Software and Systems*, Jacoby, G., Barnes, J., eds., ASP Conf. Series Vol. 101, p. 17
Bevington, P. R. 1969, Data Reduction and Error Analysis for the Physical Sciences (New York: McGraw-Hill)
Bianchi, S., Matt, G., Nicastro, F., Porquet, D. & Dubau, J. 2005, MNRAS, 357, 599
Blustin, A.J., Page, M.J., Fuerst, S.V., Branduardi-Raymont, G. & Ashton, C.E. 2005, A&A, 431, 111
Chartas, G., Brandt, W.N., Gallagher, S.C. & Garmire, G. 2002, ApJ, 579, 163
Chartas, G., Brandt, W.N. & Gallagher, S.C. 2003, ApJ, 595, 85
De Grandi, S. & Molendi, S. 2002, ApJ, 567, 163
Dickey, J. & Lockman, F. 1990, ARAA, 28, 215
Done, C., Madejski, G. & Życki, P. 2000, ApJ, 536, 213
Dove, J., Wilms, J., Maisack, M. & Begelman, M. 1997, ApJ, 487, 759
Edelson, R. & Nandra, K. 1999, ApJ, 514, 682
Esin, A., McClintock, J. & Narayan R., 1997, ApJ, 489, 865
Fabian, A.C. et al. 1989, MNRAS, 238, 729
Freyberg, M. et al. 2004, SPIE, 5165, 112
George, I.M. & Fabian, A.C. 1991, MNRAS, 249, 352
Ghisellini, G., Haardt, F. & Matt, G. 2004, A&A, 413, 535
Gondoin, P. et al. 2001, A&A, 378, 806
Grevesse, N. & Sauval, A.J. 1998, Space Science Reviews, 85, 161
Haardt, F., Maraschi, L. & Ghisellini, G. 1994, ApJ, 432, L95
Hasinger, G., Schartel, N. & Komossa, S. 2002, ApJ, 573, L77
Katayama, H., Takahasi, I., Ikebe, Y., Matsushita, K. & Freyberg, M. 2004, A&A, 414, 767
Laor, A. 1991, ApJ, 376, 90
Magdziarz, P. & Zdziarski, A. 1995, MNRAS, 273, 837
Markowitz, A. et al. 2003, ApJ, 593, 96
Markowitz, A., Edelson, R. & Vaughan, S. 2003, ApJ, 598, 935
Matt, G. 2002, MNRAS, 337, 147
McKernan, B. & Yaqoob, T. 2004, ApJ, 608, 157
McKernan, B., Yaqoob, T. & Reynolds, C.S. 2004, ApJ, 617, 232
Narayan, R. & Yi, I. 1995, ApJ, 444, 231
Nevalainen, J., Oosterbroek, T., Bonamente, M. & Colafrancesco, S. 2004, ApJ, 608, 166
Nikolajuk, M., Papadakis, I. & Czerny, B. 2004, MNRAS, 350, L26
Perola, G.C., Matt, G. & Cappi, M. 1999, A&A, 351, 937
Peterson, B.M. et al. 2004, ApJ, 613, 682
Porquet, D., Reeves, J.N., Uttley, P. & Turner, T.J. 2004, A&A, 427, 101
Pounds, K.A., Reeves, J.N., King, A.R., Page, K.L., O'Brien, P.T. & Turner, M.J.L. 2003a, MNRAS, 345, 705
Pounds, K.A., King, A.R., Page, K.L. & O'Brien, P.T. 2003b, MNRAS, 346, 1025
Pounds, K.A. & Page, K.L. 2005, MNRAS, 360, 1123
Protassov, R., van Dyk, D.A., Connors, A., Kashyap, V.L. & Siemiginowska, A. 2002, ApJ, 571, 545
Reeves, J.N., O'Brien, P.T. & Ward, M. 2003, ApJ, 593, L65
Reeves, J.N., Nandra, K., George, I.M., Pounds, K.A., Turner, T.J. & Yaqoob, T. 2004, ApJ, 602, 648
Revnivtsev, M., Sazonov, S., Jahoda, K. & Gilfanov, M. 2004, A&A, 418, 927
Rothschild, R. et al. 1998, ApJ, 496, 538
Steenbrugge, K.C., Kaastra, J.S., Sako, M., Branduardi-Raymont, G., Behar, E., Paerels, F.B.S., Blustin, A.J. & Kahn, S. 2005, A&A 432, 453
Tanaka, Y. et al. 1995, Nature, 375, 659
Turner, T.J. et al.2005, ApJ, 618, 155
Vaughan, S., Edelson, R., Warwick, R. & Uttley, P. 2003, MNRAS, 345, 1271
Wandel, A., Peterson, B.M. & Malkan, M. 1999, ApJ, 526, 579
Weaver, K., Gelbord, J. & Yaqoob, T. 2001, ApJ, 550, 261
Wilms, J. et al. 2001, MNRAS, 328, L27
Yaqoob, T., George, I.M., Kallman, T., Padmanabhan, U., Weaver, K. & Turner, T.J. 2003, ApJ, 596, 85
Yaqoob, T. & Padmanabhan, U. 2004, ApJ, 604, 63
Young, A.J. et al. 2005, ApJ, 631, 733

TABLE 1

JOINT PCA/HEXTE FITTING RESULTS FOR MODEL 3: POWER-LAW + PEXRAV + GAUSSIAN

Parameter	Long-term	Med-term
χ^2/dof	208.14/123	82.7/101
2–10 keV flux (erg cm^{-2} s^{-1})	1.20×10^{-10}	1.12×10^{-10}
25–100 keV flux (erg cm^{-2} s^{-1})	1.78×10^{-10}	1.74×10^{-10}
Γ	$1.894^{+0.013}_{-0.015}$	$1.782^{+0.012}_{-0.021}$
R	0.51 ± 0.04	$0.35^{+0.05}_{-0.11}$
E (keV)	$6.38^{+0.05}_{-0.02}$	6.33 ± 0.03
σ (eV)	228 ± 50	341 ± 54
I (10^{-5} ph cm^{-2} s^{-1})	$18.2^{+1.4}_{-1.1}$	25.3 ± 1.9
EW (eV)	128^{+10}_{-8}	197 ± 15

Note. — Model parameters for the best-fitting Model 3 (power-law + PEXRAV + Gaussian) to the PCA/HEXTE data. Errors are 90% confidence for one interesting parameter. E, σ, K, and EW are the centroid energy, width, intensity and equivalent width for the Fe Kα Gaussian emission component. Fe Kβ line emission was not considered here. The high-energy cutoff in the PEXRAV component was fixed at 270 keV (e.g., Perola et al. 1999); the inclination was kept fixed at 30 degrees. The 25–100 keV flux is based on average of HEXTE cluster A and B model fluxes.

TABLE 2

INITIAL EPIC-PN MODEL FITS FOR FE K EMISSION LINES

		Model 1	Model 2	Model 3	Model 4	Model 5
χ^2/dof		2822.59/1896	1945.40/1893	1865.73/1893	1844.88/1890	1852.78/1893
Γ		$1.656^{+0.015}_{-0.011}$	$1.671^{+0.012}_{-0.015}$	1.737 ± 0.012	1.743 ± 0.013	1.742 ± 0.013
Red peak	E (keV)	...	6.40 ± 0.01	6.40 ± 0.01	6.39 ± 0.01	6.40 ± 0.01
	σ_1	...	106 ± 14	91 ± 15	91 ± 13	93^{+15}_{-13}
	$I_{\rm K\alpha}$	...	8.8 ± 0.7	$7.8^{+0.4}_{-0.6}$	$8.0^{+0.6}_{-0.7}$	8.0 ± 0.6
	$EW_{\rm K\alpha}$ (eV)	...	86 ± 6	75^{+4}_{-6}	76^{+6}_{-7}	77 ± 6
Blue peak	E (keV)	...	...	...	$6.93^{+0.07}_{-0.09}$	7.06 (fixed)
	σ_2	...	...	...	121^{+95}_{-59}	$(=\sigma_1)$
	$I_{\rm K\beta}$	...	...	...	$1.3^{+0.7}_{-0.5}$	$(= 0.11 * I_{K\alpha})$
	$EW_{\rm K\beta}$ (eV)	...	...	...	15^{+8}_{-6}	$(= 0.11 * EW_{K\alpha})$

Note. — Line intensities are in units of 10^{-5} ph cm^{-2} s^{-1}. A PEXRAV component was included in all models except 1 and 2, with reflection strength R fixed at 0.51. 2–10 keV flux for Models 4–5 was 8.92×10^{-11} erg cm^{-2} s^{-1}.

TABLE 3

EPIC-PN MODEL FITS: ATTEMPTS TO MODEL COMPTON SHOULDER EMISSION

		Model 6A	Model 6B
χ^2/dof		1839.03/1889	1833.68/1888
Γ		1.743 ± 0.012	1.744 ± 0.012
Red peak	E (keV)	6.41 ± 0.01	6.40 ± 0.01
	σ_1	71^{+17}_{-14}	76^{+24}_{-19}
	$I_{K\alpha}$ (10^{-5} ph cm^{-2} s^{-1})	6.7 ± 0.9	$7.4^{+1.1}_{-1.0}$
	$EW_{\rm K\alpha}$ (eV)	63 ± 8	70^{+11}_{-9}
Blue peak	E (keV)	7.06 (fixed)	7.06 (fixed)
	σ_2	$(=\sigma_1)$	$(=\sigma_1)$
	$I_{K\beta}$ (10^{-5} ph cm^{-2} s^{-1})	$(= 0.11 * I_{K\alpha})$	$(= 0.11 * I_{K\alpha})$
	$EW_{\rm K\beta}$ (eV)	$(= 0.11 * EW_{\rm K\alpha})$	$(= 0.11 * EW_{\rm K\alpha})$
Compton shoulder	E (keV)	6.24 (fixed)	$6.13^{+0.07}_{-0.25}$
	σ_2	$(=\sigma_1)$	$(=\sigma_1)$
	I (10^{-5} ph cm^{-2} s^{-1})	1.4 ± 0.8	1.1 ± 0.5
	EW (eV)	11 ± 8	9 ± 5

Note. — A PEXRAV component was included, with reflection strength R fixed at 0.51. A comparison of these models with the dual-diskline model suggests that the excess residual emission on the red side of the Kα core is emission due to the red wing of a moderately broadened diskline profile, and not a Compton shoulder.

TABLE 4

EPIC-PN MODEL FITS USING A SINGLE DISKLINE COMPONENT (MODEL 7)

χ^2/dof	1922.56/1893
Γ	1.739 ± 0.013
E (keV)	6.40 ± 0.01
I (10^{-5} ph cm^{-2} s^{-1})	$8.6^{+0.5}_{-0.6}$
EW	84^{+6}_{-6}
β	6 (unconstrained)
$R_{\rm in}$	300^{+100}_{-270}
Incl.	30° (fixed)

Note. — For the LAOR diskline component, the outer radius was kept fixed at 400 $R_{\rm g}$. Results are presented here for an inclination angle of 30°; angles of 50° or 70° yielded significantly worse fits. A PEXRAV component with R=0.51 was included.

TABLE 5

EPIC-PN MODEL FITS USING DUAL DISKLINE COMPONENTS (MODEL 8)

χ^2/dof		1835.23/1890
Γ		1.741 ± 0.013
Red peak	E (keV)	6.44 ± 0.01
	I (10^{-5} ph cm^{-2} s^{-1})	$8.9^{+1.7}_{-0.8}$
	EW	86^{+17}_{-8}
Blue peak	E (keV)	6.98 ± 0.09
β		2.1 ± 0.3
$R_{\rm in}$		$13^{+13}_{-11.8}$
Incl.		$1^{+11\circ}_{-1}$

Note. — For each LAOR diskline component, the outer radius was kept fixed at 400 $R_{\rm g}$. The normalization of the blue peak diskline was kept fixed at 0.11 times that of the red peak. A PEXRAV component with R=0.51 was included.

TABLE 6

EPIC-PN MODEL FITS USING DUAL-DISKLINES AND DUAL-GAUSSIANS (MODELS 9A AND 9B)

			Model 9A	Model 9B
χ^2/dof			1833.82 / 1889	1835.44 / 1888
Γ			1.741 ± 0.013	1.743 ± 0.013
Gaussians	Red peak	E (keV)	6.40 (fixed)	6.39 ± 0.01
		$I_{\rm K\alpha,narrow}$	$2.5^{+3.4}_{-2.5}$	$6.1^{+1.1}_{-6.1}$
		$EW_{\rm K\alpha,narrow}$ (eV)	22^{+30}_{-22}	56^{+10}_{-56}
	Blue peak	E (keV)	7.06 (fixed)	7.06 (fixed)
	σ		50 (fixed)	66^{+19}_{-22}
LAOR Disklines	Red peak	E (keV)	$6.44^{+0.19}_{-0.15}$	$6.30^{+0.40}_{-0.22}$
		$I_{\rm K\alpha,broad}$	6.3±3.0	4.0±1.8
		$EW_{\rm K\alpha,broad}$ (eV)	59±28	37±17
	Blue peak	E (keV)	$6.96^{+0.12}_{-0.41}$	7.06 (fixed)
	β		$2.6^{+1.4}_{-0.8}$	$1.8^{+2,4}_{-1.6}$
	$R_{\rm in}$		$19^{+45}_{-18.8}$	1.2^{+80}_{-0}
	i		11^{+19}_{-11}	$45^{+19\circ}_{-41}$

Note. — Best-fit spectral parameters for a model in which the red peak (Fe Kα) and blue peak (Fe Kβ) are each modeled by the sum of a narrow Gaussian and a broad LAOR diskline. The widths σ of the two Gaussians were tied. The intensity of the blue peak Gaussian was kept fixed at 17/150 that of the red peak Gaussian. The inner radii $R_{\rm in}$, emissivity index β and inclination i of the two diskline components were kept tied. The outer radii of both disklines were kept fixed at 400 $R_{\rm g}$. Line intensities are in units of 10^{-5} ph cm^{-2} s^{-1}. The intensity of the blue peak diskline was kept fixed at 17/150 that of the red peak diskline. To get a reasonable fit, the centroid energy of the Kβ Gaussian and the rest energy of the Kβ diskline were both kept fixed at 7.06 keV. A PEXRAV component with R=0.51 was included in the model. The 2–10 keV flux for the best-fit model was 8.9×10^{-11} erg cm^{-2} s^{-1}.

TABLE 7
EPIC-PN MODEL FITS FOR 7.68 KEV ABSORPTION FEATURE

		Model 10	Model 11	Model 12	Model 13
χ^2/dof		1829.70/1889	1819.20/1898	1813.50/1887	1809.17/1887
Γ		$1.746^{+0.013}_{-0.012}$	$1.715^{+0.014}_{-0.006}$	1.734± 0.012	$1.728^{+0.014}_{-0.009}$
Red peak	E (keV)	6.44±0.01	6.44±0.01	6.44±0.01	6.44±0.01
	I (10^{-5} ph cm^{-2} s^{-1})	$8.7^{+0.9}_{-0.8}$	8.0±0.7	$8.5^{+0.9}_{-0.7}$	$8.3^{+0.9}_{-0.6}$
	EW (eV)	83^{+9}_{-7}	76±6	81^{+8}_{-7}	79^{+8}_{-6}
Blue peak	E (keV)	$6.98^{+0.07}_{-0.11}$	$6.98^{+0.11}_{-0.10}$	6.98±0.09	6.98±0.09
β		$2.1^{+0.4}_{-0.3}$	$2.1^{+0.2}_{-0.6}$	$2.1^{+0.4}_{-0.3}$	$2.1^{+0.4}_{-0.3}$
$R_{\rm in}$		$13^{+13}_{-11.8}$	$17^{+26}_{-15.8}$	$15^{+17}_{-13.8}$	$16^{+13}_{-14.8}$
Incl.		$3^{+9\circ}_{-3}$	$0^{+10\circ}_{-0}$	$0^{+12\circ}_{-0}$	$0^{+10\circ}_{-0}$
PEXRIV	logξ (erg cm s^{-1})	<0.04	...	...	...
Edge	E (keV)	...	$7.29^{0.25}_{-0.17}$	...	...
	optical depth τ	...	0.034 ± 0.013	...	...
Gaussian	E (keV)	...	...	$7.68^{+0.04}_{-0.03}$	...
	σ	...	...	35^{+65}_{-35}	...
	$\mid I \mid$ (10^{-5} ph cm^{-2} s^{-1})	...	...	1.0±0.3	...
	$\mid EW \mid$ (eV)	...	...	13±5	...
Photoionized Abs.	Col. dens. (cm^{-2})	...	...	...	$1.4^{+1.0}_{-0.5} \times 10^{22}$
	log ξ (UNITS)	...	...	...	3.73 ± 0.13
	z (rel. to systemic)	...	...	...	$-0.093^{+0.006}_{-0.002}$

Note. — Spectral parameters for best-fit models which attempt to model the 7.68 keV absorption feature. See text for details.

TABLE 8
MODEL 12 FITS TO EACH HALF OF THE EPIC-PN SPECTRUM

		First half	Second half
F_{2-10} (erg cm^{-2} s^{-1}		9.4×10^{-11}	9.2×10^{-11}
χ^2/dof		1883.15/1887	1933.52/1887
Γ		$1.787^{+0.031}_{-0.013}$	$1.776^{+0.022}_{-0.017}$
Red peak	E (keV)	$6.44^{+0.02}_{-0.01}$	$6.45^{+0.02}_{-0.01}$
	I (10^{-5} ph cm^{-2} s^{-1})	$8.0^{+0.9}_{-0.8}$	$8.3^{+0.9}_{-0.7}$
	EW (eV)	73^{+8}_{-7}	77±8
Blue peak	E (keV)	$7.03^{+0.10}_{-0.13}$	$7.03^{+0.10}_{-0.12}$
β		$2.6^{+0.6}_{-1.0}$	$2.0^{+0.3}_{-0.6}$
$R_{\rm in}$		44±19	20^{+27}_{-11}
Incl.		$10^{+8\circ}_{-10}$	$0^{+9\circ}_{-0}$
Gaussian	E (keV)	$7.68^{+0.06}_{-0.09}$	$7.68^{+0.08}_{-0.06}$
	σ	53^{+127}_{-53}	18^{+162}_{-18}
	$\mid I \mid$ (10^{-5} ph cm^{-2} s^{-1})	$1.3^{+0.8}_{-0.7}$	$0.8^{+0.6}_{-0.5}$
	$\mid EW \mid$ (eV)	16^{+10}_{-9}	10^{+8}_{-6}
	F-test to include	99.6%	92.8%

Note. — Best-fitting model 12, featuring dual-disklines for the Fe K emission peaks and an inverted Gaussian for the 7.68 keV absorption feature, to the first and second halves of the EPIC-pn data. All spectral parameters are consistent with remaining constant over timescales <136 ksec. The final row shows the level of significance to include the inverted Gaussian according to an F-test used in the 'standard' manner (see text for details).

TABLE 9

F-TEST RESULTS TO THAW Γ OR I_{Fe} IN THE TIME-RESOLVED FITS

Time Scale	Γ F	Γ Prob	I_{Fe} F	I_{Fe} Prob
Short	0.35	0.95	0.02	1.00
Medium	5.53	2.3×10^{-12}	1.51	7.8×10^{-2}
Long	3.04	2.3×10^{-5}	2.28	1.9×10^{-3}

Note. — Results of F-tests to determine which parameters it was significant to thaw in the time-resolved fits. High values of the F-statistic and low-values of the probability (of observing that value of F from a random set of data) indicate that the fits show improvement to thaw that parameter, suggesting statistically significant variations.

TABLE 10

MEAN SPECTRAL FIT VARIABILITY PARAMETERS AND ERRORS

Time Scale	Mean F_{2-10} 10^{-11} ph cm^{-2} s^{-1}	Mean Γ	Mean I_{Fe} 10^{-5} ph cm^{-2} s^{-1}	Γ r	Γ Prob	I_{Fe} r	I_{Fe} Prob
Short	9.91±0.12	1.822±0.029	8.30±0.76	0.803	1.6×10^{-2}	–0.106	0.80
Medium	13.29±0.06	1.828±0.033	20.47±3.43	0.819	3.2×10^{-5}	0.272	0.27
Long	15.62±0.09	1.917±0.067	16.60±4.12	0.656	3.1×10^{-3}	–0.059	0.82

Note. — Mean values of F_{2-10}, Γ and I_{Fe}. See text for details on error calculations. The Pearson correlation coefficients r in Columns (4) and (6) are for Γ and I_{Fe}, respectively, plotted against F_{2-10}, as shown in Figure 11. The corresponding null hypothesis probabilities (of achieving that value of r from a random set of data) are listed in Columns (5) and (7). See §4.4 for notes relating PCA and pn flux normalizations.

TABLE 11

F_{var} VALUES

Time Scale	Continuum F_{var} (%)	Line F_{var} (%)
Short	3.50 ± 0.45	Undef.
Medium	9.34 ± 0.14	3.49 ± 13.99
Long	12.99 ± 0.17	5.54 ± 19.42

Note. — Undefined fractional variability measurements indicate a measured variance that is smaller than that expected solely from measurement noise.

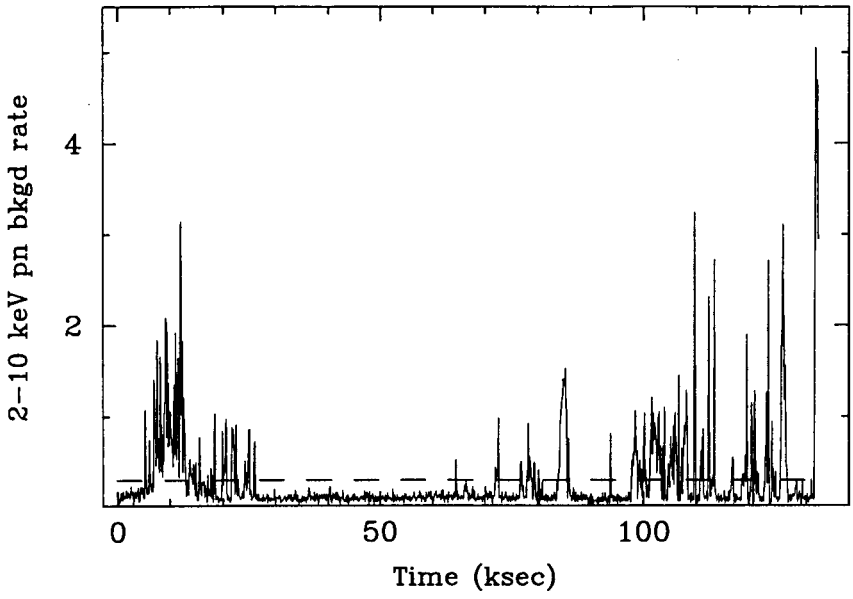

FIG. 1.— 10–12 keV pn background light curve. The dotted line at 0.3 count s^{-1} corresponds to a count rate of $B + 2\sigma$, where B is the mean background rate and σ is the standard deviation of the light curve. We tested for background contamination by filtering out data taken when the background count rate exceeded this threshold. However, we found no impact on the Fe K profile, the focus of this paper, and used the unfiltered data for maximum signal-to-noise in the analysis.

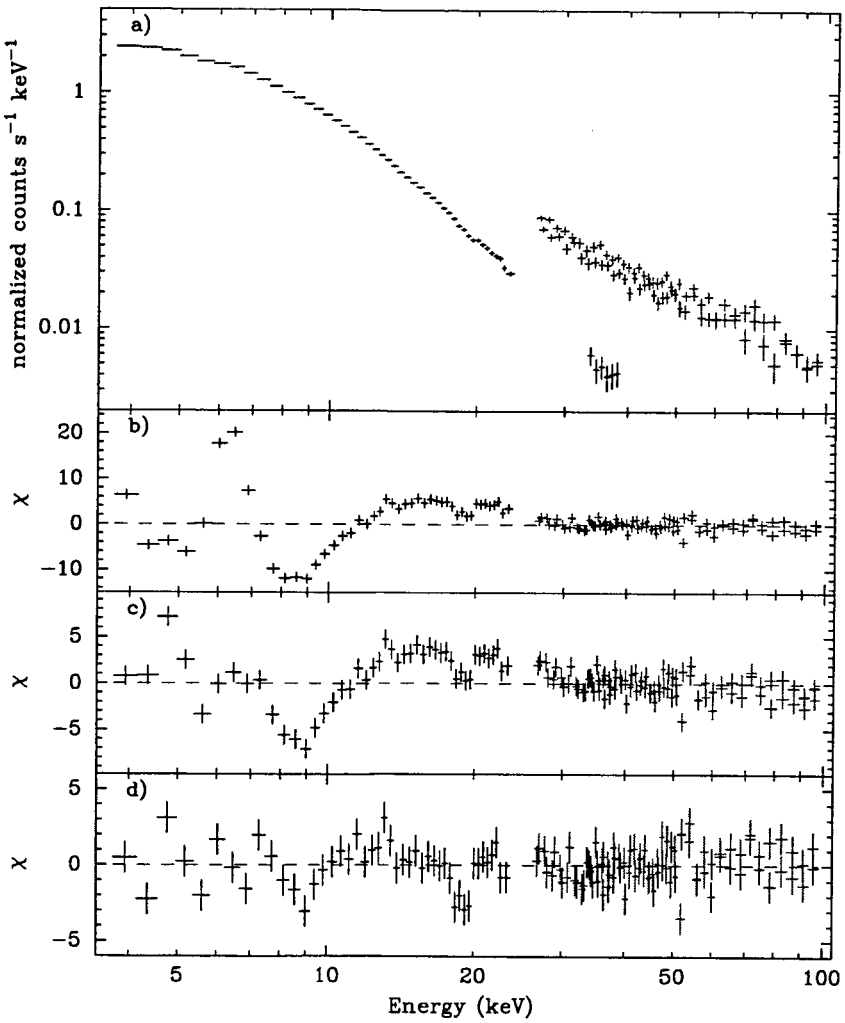

FIG. 2.— Panel a) shows the *RXTE* PCA, HEXTE A cluster and HEXTE B cluster spectra, in black, red and blue, respectively. Panel b) shows the data/model residuals when the data are fit with Model 1, an absorbed power-law model. Panel c) shows the residuals when a Gaussian is included to model Fe K emission (Model 2). Panel d) shows the residuals when a PEXRAV reflection component is also included. For clarity in panels b), c), and d), residuals in χ-space are plotted (typical uncertainties on the HEXTE data/model ratio points were ± 0.2 and so data/model ratios are not plotted).

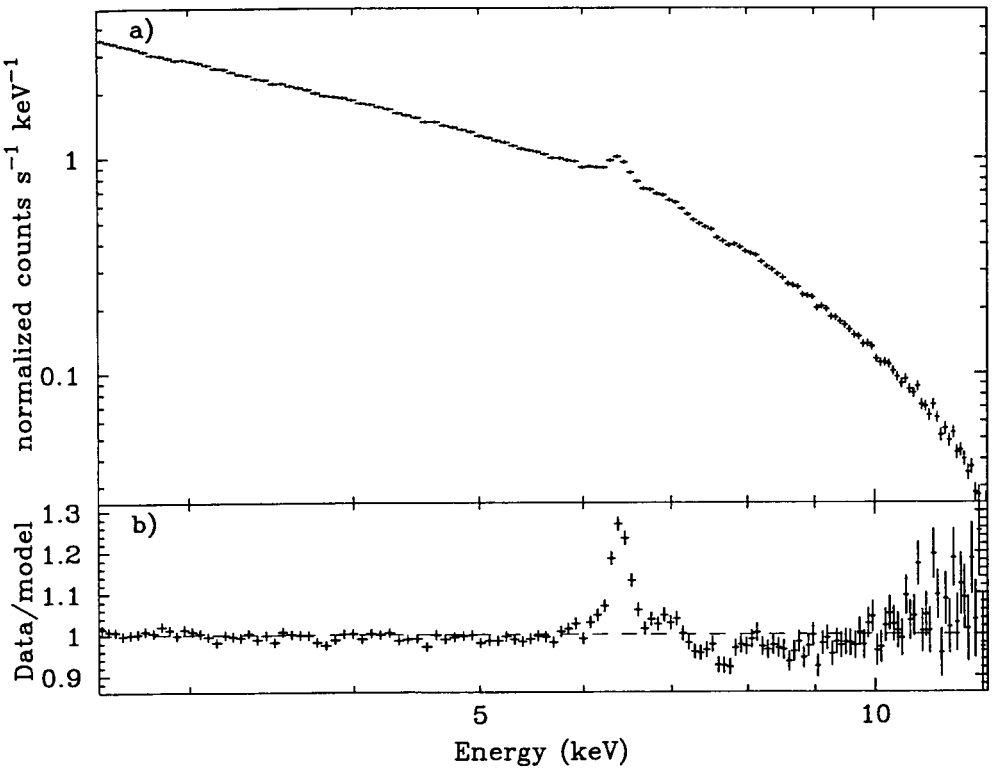

FIG. 3.— Panel a) shows the 2.5–12 keV EPIC pn spectrum, with a binning factor of 15. Panel b) shows the data/model residuals when a simple absorbed power-law model is fit (Model 1). Large residuals in the Fe K bandpass are present.

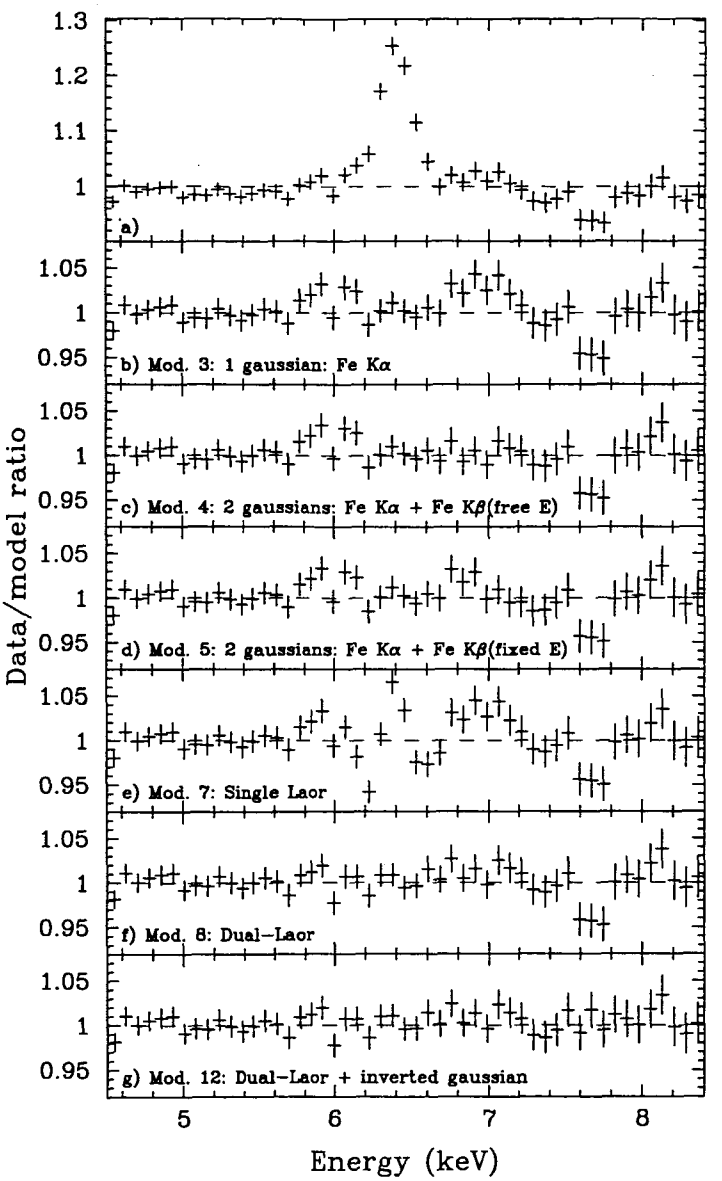

FIG. 4.— Data/model residuals in the Fe K bandpass when various models are fit to the EPIC pn data. All plots here denote models which include a power-law and a PEXRAV reflection component with R fixed at −0.51, with all components modified by neutral absorption. Data have been rebinned by a factor of 15. Panel a) shows the residuals using just the power-law and PEXRAV component (e.g., the ∼7.1 keV edge has been fit compared to the residuals in Figure 3b). Panel b) shows the residuals to Model 3, which included a Gaussian to model Fe Kα emission. Panels c) and d) show the residuals to Models 4 and 5, double Gaussian models for the Fe Kα and Kβ emission lines. The energy centroid for the Kβ line was free in Model 4, but fixed at 7.06 keV in Model 5. Panel e) shows the residuals to Model 7, an attempt to model both peaks with a single LAOR diskline component; there are large residuals suggesting a poor fit to the data. Panel f) shows the residuals to Model 8, wherein each peak was modeled with a separate LAOR component. Note that the residuals near 5.8–6.1 keV and 6.7–6.9 keV are improved compared to Model 5, suggesting that the dual-LAOR model is fitting red wing emission unmodeled by the double-Gaussian model (see text for quantification of this statement). Note also that the absorption-like residuals near 7.68 keV are unchanged in panels a)–f), suggesting that the absorption feature persists regardless of how the emission profile is modeled. Panel g) shows the residuals to Model 12, which features dual-LAOR disklines to model the emission lines and a narrow inverted Gaussian to model the 7.68 keV absorption feature.

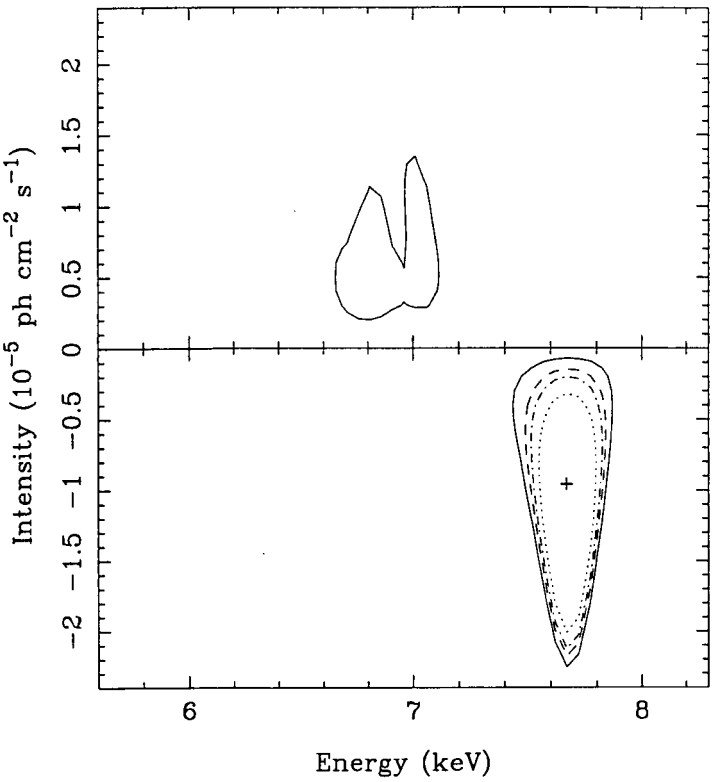

FIG. 5.— Derived confidence contours of line intensity versus rest-frame energy when a narrow Gaussian is added to Model 8, the dual-LAOR diskline model. The upper panel is for a Gaussian in emission, and suggests there is no additional emission (at 90% confidence or greater) to be modeled. The lower panel is for a Gaussian in absorption, and suggest (at >99% confidence) a narrow absorption feature at 7.68 keV. Solid, dashed, dashed-dotted, and dotted lines denote 68%, 90%, 95% and 99% confidence levels, respectively. The best-fitting parameters to Model 11 are marked with a cross.See text for details.

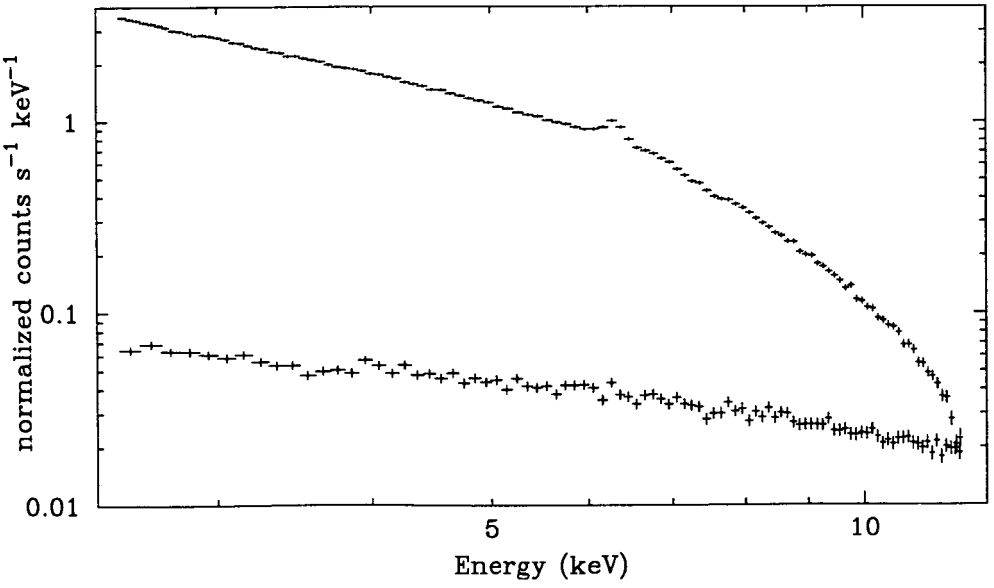

FIG. 6.— The pn source (top) and background (bottom) spectra, rebinned by a factor of 20, showing that the source is well over an order of magnitude higher in counts s^{-1} keV^{-1} compared to the background in the Fe K bandpass.

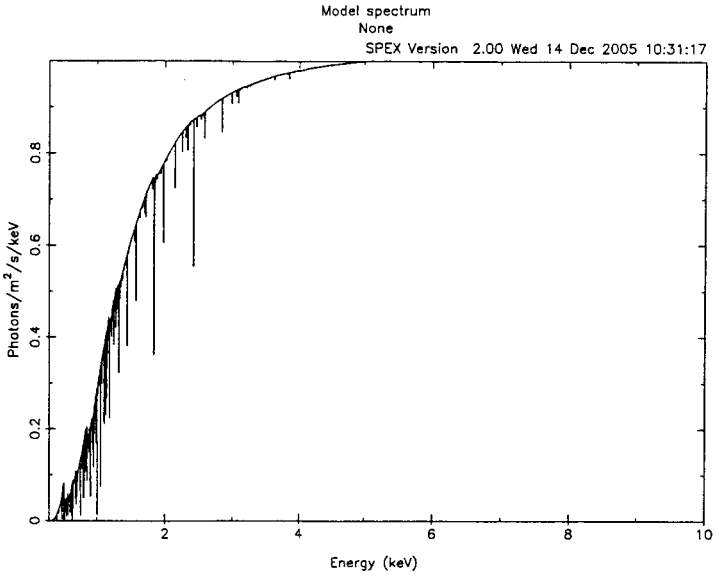

FIG. 7.— The effect of the total absorption from all the soft X-ray absorbers in S05 on a simple power-law, normalized to ~1 at high energies is shown. There is a negligible effect at energies above ~4 keV. Based on the soft X-ray absorption modeling, no strong absorption lines in the Fe K bandpass are expected. (courtesy of K. Steenbrugge)

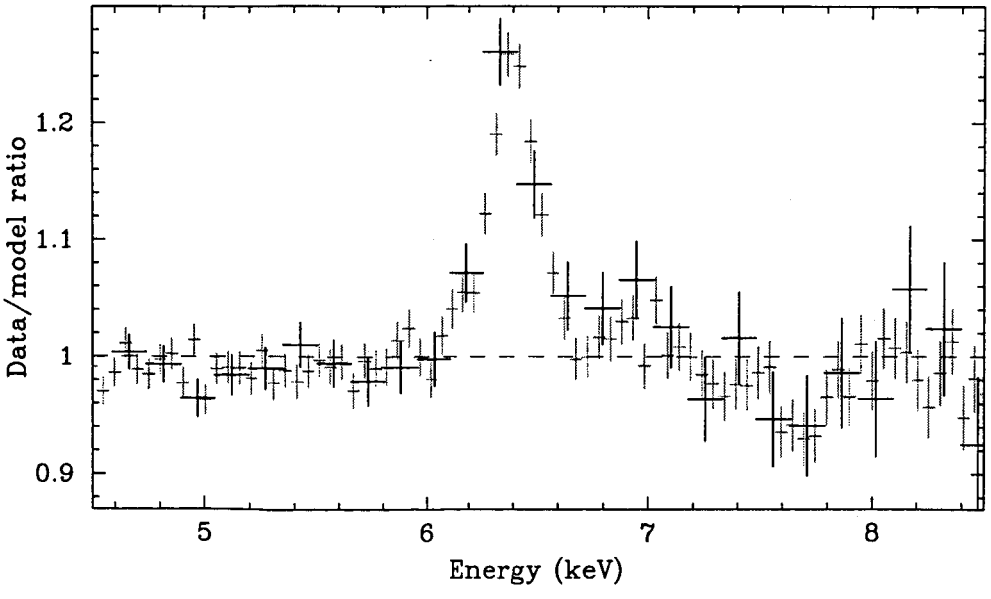

FIG. 8.— Data/model residuals to a simple absorbed power-law (rebinned by a factor of 10) for the MOS2 (black) and pn (grey), showing that the MOS2 data are consistent with the pn.

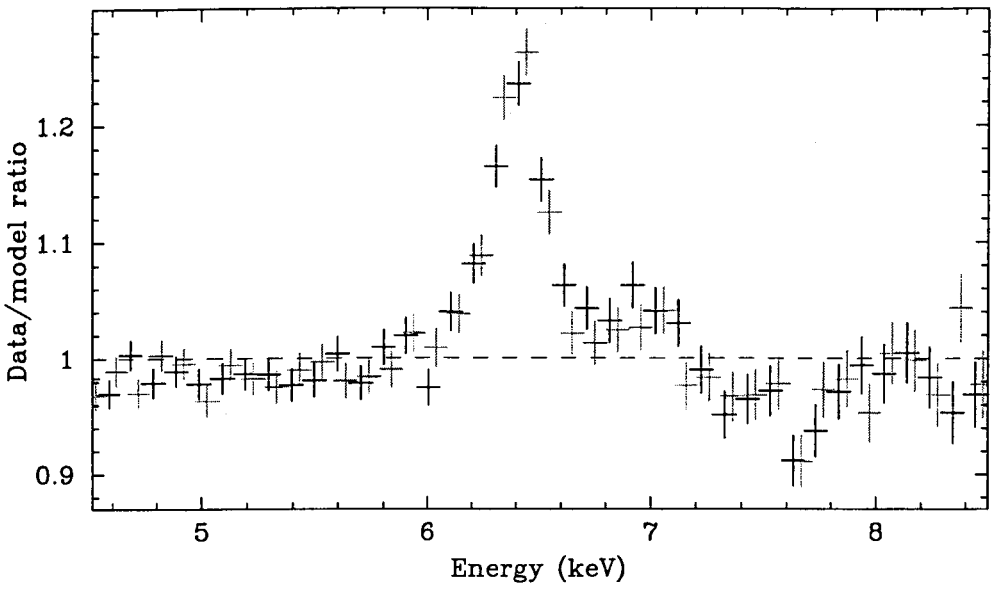

FIG. 9.— Data/model residuals for the first half (black) and second half (gray) of the pn data when fitting to a model consisting of a power-law and a PEXRAV reflection component, all modified by neutral absorption. All derived spectral parameters are consistent with each other, suggesting no evidence that the profile varies on short time scales.

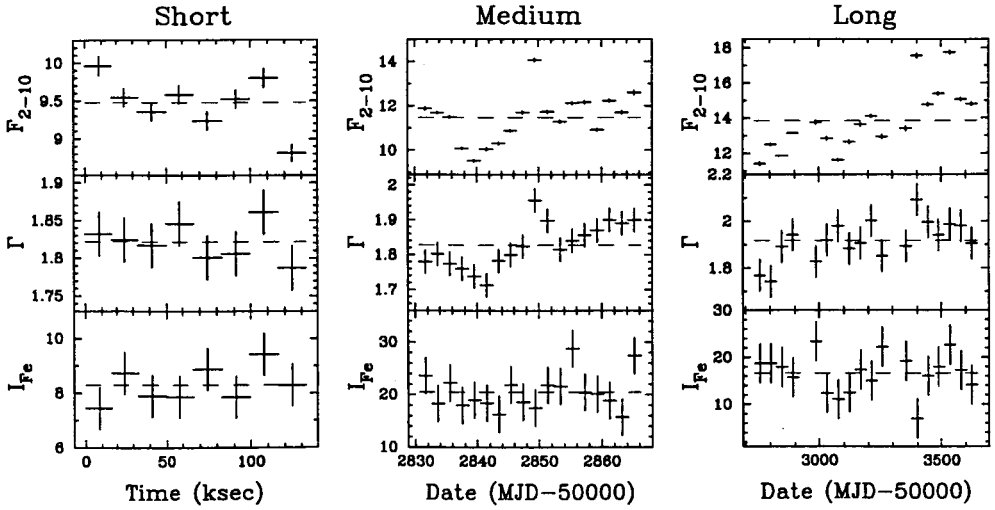

FIG. 10.— Light curves for the 2–10 keV continuum flux F_{2-10} (top), photon index Γ (middle), and Fe K flux $I_{\rm Fe}$ (bottom) for all three time scales, derived from time-resolved spectroscopy. F_{2-10} is in units of 10^{-11} erg cm^{-2} s^{-1}. $I_{\rm Fe}$ is in units of 10^{-5} ph cm^{-2} s^{-1}.

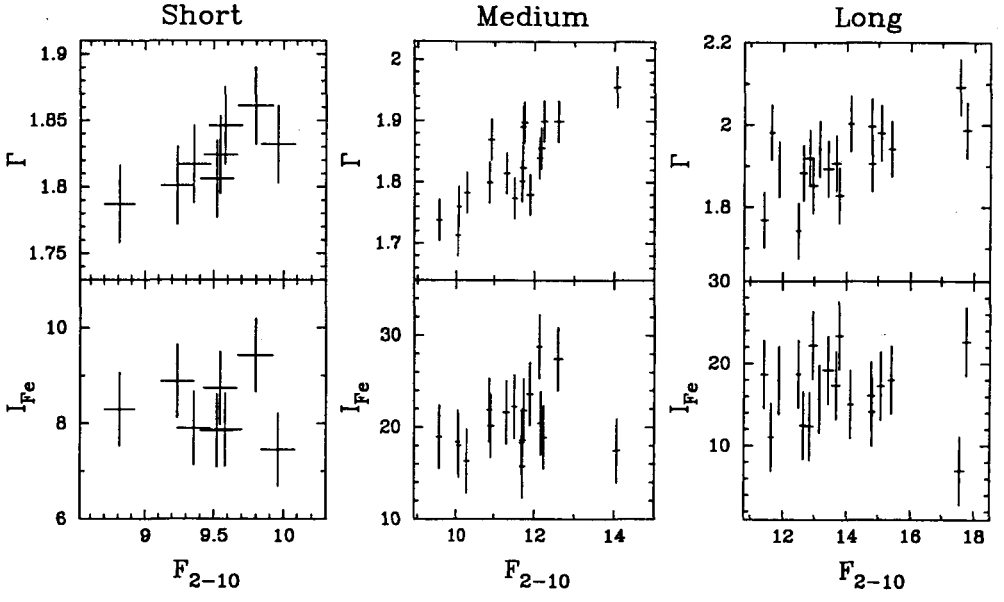

FIG. 11.— Photon index Γ (top) or Fe K flux I_{Fe} (bottom) plotted against 2–10 keV continuum flux F_{2-10} for all three time scales, derived from time-resolved spectroscopy. F_{2-10} is in units of 10^{-11} erg cm^{-2} s^{-1}. I_{Fe} is in units of 10^{-5} ph cm^{-2} s^{-1}. These plots, along with Figure 10 and Tables 10 and 11, suggest that temporal variations in Γ are well-correlated with those in F_{2-10} on all three time scaled studied, but there is not strong evidence for I_{Fe} to vary on any of the time scales studied. See text for details.